

Chromatic Afterglow of GRB 200829A

N. S. Pankov,^{1,2*} A. S. Pozanenko,² P. Yu. Minaev,^{2,3} S. O. Belkin,^{1,2} A. A. Volnova,² I. V. Reva,⁴ A. V. Serebryanskiy,⁴ M. A. Krugov,⁴ S. A. Naroenkov,⁵ A. O. Novichonok,⁶ A. A. Zhornichenko,⁶ V. V. Rumyantsev,⁷ K. A. Antonyuk,⁷ Sh. A. Egamberdiev,⁸ O. A. Burkhonov,⁸ E. V. Klunko,⁹ A. S. Moskvitin,¹⁰ I. E. Molotov,¹¹ R. Ya. Inasaridze¹²

¹National Research Institute "Higher School of Economics", ul. Myasnitskaya 21/4, build. 5, Moscow 101000, Russia

²Space Research Institute, Russian Academy of Sciences, ul. Profsoyuznaya 84/32, Moscow 117997, Russia

³Lebedev Physical Institute, Russian Academy of Sciences, Leninskiy Prospekt 53, Moscow 119991, Russia

⁴Fesenkov Astrophysical Institute, Observatory 23, Almaty 05002, Kazakhstan

⁵Institute of Astronomy, ul. Pyatnitskaya 48, Moscow 119017, Russia

⁶Petrozavodsk State University, Prospekt Lenina 33, Petrozavodsk 185035, Republic of Karelia, Russia

⁷Crimean Astrophysical Observatory, p. Nauchny 185035, Republic of Crimea, Russia

⁸Mirzo Ulug'bek nomidagi Astronomiya instituti, Astronomicheskaya str. 33, Toshkent 100052, O'zbekiston

⁹Institute of Solar-Terrestrial Physics, Russian Academy of Sciences, Siberian Branch, ul. Lermontova 126a, Irkutsk 664033, Russia

¹⁰Special Astrophysical Observatory, Russian Academy of Sciences, Nizhnii Arkhyz 369167, Karachai-Cherkessian Republic, Russia

¹¹Keldysh Institute of Applied Mathematics, Miusskaya Ploshchad' 4, Moscow 125047, Russia

¹²Evgeni Kharadze Georgian National Astrophysical Observatory, Abastumani 0301, Georgia

7 August 2023

Abstract

We present the results of our analysis of multiwavelength observations for the long gamma-ray burst GRB 200829A. The burst redshift $z \approx 1.29 \pm 0.04$ has been determined photometrically at the afterglow phase. In gamma rays the event is one of the brightest (in isotropic equivalent), $E_{iso} \gtrsim 10^{54}$ erg. The multicolor light curve of the GRB 200829A afterglow is characterized by chromatic behavior and the presence of a plateau gradually transitioning into a power-law decay that can also be interpreted as a quasi-synchronous inhomogeneity (flare). We assume that the presence of a chromatic inhomogeneity in the early afterglow is consistent with the model of a structured jet.

Keywords: gamma-ray bursts, afterglow, photometric observations, optical transients

1 INTRODUCTION

The cosmological nature of gamma-ray bursts (GRBs) proposed at the beginning of their studies (Prilutskii & Usov 1975; Paczynski 1986) has been confirmed by measuring their redshifts. The median redshift for long bursts is $z_{med} = 1.67$ (see, e.g., Daigne et al. 2006; Tsvetkova et al. 2017, 2021). At the same time, the fraction of events with redshifts directly measured through optical spectroscopic observations is $\sim 5\%$ of events (Kaneko et al. 2006; Butler et al. 2007; Lien et al. 2016; von Kienlin et al. 2020). There are other known z estimation methods, for example, modeling the photometric afterglow magnitudes (Schady et al. 2010), the spectroscopic or photometric method of modeling broadband host galaxy spectra (see, e.g., Volnova et al. 2014).

Long GRBs are associated with the core collapse of massive stars (Colgate 1968; Bisnovaty-Kogan et al. 1975; Woosley 1993; Paczyński 1998) and, as a rule, a supernova (SN) is detected in $\sim 10\%$ of the events with a registered optical component, for example, SN 1998bw, SN 2003dh, SN 2013dx, and GRB 181201A (Wang & Wheeler 1998; Woosley et al.

1999; Mazzali et al. 2003; Volnova et al. 2017; Belkin et al. 2020). However, it is difficult to detect an SN for GRBs at $z \gtrsim 1$, since it becomes too faint. The farthest SN from GRBs was associated with GRB 000911 at $z = 1.06$ (Lazzati et al. 2001; Masetti et al. 2005).

The color evolution between optical and X-ray afterglow light curves detected, for example, for GRB 050525A (Oates et al. 2011; Resmi et al. 2012) and GRB 130831A (De Pasquale et al. 2016) is not explained by the standard afterglow model (Sari et al. 1999; Piran 2004; Kumar & Zhang 2015). The afterglow light curve in the standard model decays monotonically (as a power law with an exponent close to unity) and synchronously in the optical and X-ray bands. The chromaticity is explained, for example, using the model of a structured jet, in which the optical and X-ray emissions are simultaneously observed from different jet regions with different Lorentz factors (Beniamini et al. 2020; Lamb et al. 2021; Duque et al. 2022). The existence of a structured jet was shown to be possible in numerical simulations (see, e.g., Komissarov et al. 2009).

The X-ray flare can closely follow the flare in the GRB prompt phase, but with a lower amplitude and energy (Duque et al. 2022). The presence of a plateau on the light curve is

* E-mail: npankov@hse.ru

also associated with a small initial Lorentz factor of the jet ($\langle \Gamma_0 \rangle \sim 51$, see Dereli-Bégué et al. 2022) or the formation of a magnetar with a magnetic field $B \sim 10^{15} - 10^{16}$ G (de Pasquale et al. 2007; Metzger et al. 2011; Rowlinson et al. 2013). A correlation between the X-ray plateau duration and the burst luminosity was found by Dainotti et al. (2008, 2021, 2022). The evolution of the views about GRBs and relevant reviews can be found, for example, in Rozental et al. (1983); Luchkov et al. (1996); Postnov (1999); Levan (2018); Pozanenko et al. (2021); Yu et al. (2022).

An extensive study of GRBs in the gamma-ray, X-ray, and optical bands was initiated by the Swift observatory (Hill et al. 2006). GRB 200829A is one of the brightest GRBs detected by this observatory. The multiwavelength light curve of the early afterglow from this burst has two inhomogeneities: a plateau and a chromatic flare. The plateau can be associated with the formation of an unstable magnetar with a strong magnetic field. The chromatic behavior of the flare probably arises when observing different jet zones in the X-ray and optical bands, closer to or farther from the jet axis, respectively. The paper is organized as follows. First, we present the results of the observations with space observatories in which the GRB was detected and the first ground-based observations of its optical afterglow. Subsequently, we present the results of processing the data obtained with space gamma-ray telescopes in the burst prompt phase. GRB 200829A is one of the most powerful (in isotropic equivalent) GRBs in the energy range 1 keV–10 MeV. In the next section we provide the observational data for the afterglow in the optical and X-ray bands and construct its light curves. Their joint analysis showed the presence of a plateau and a chromatic flare in the early afterglow. Then, we present the procedure and the redshift estimate obtained by modeling the multicolor light curve of the early afterglow in the optical and X-ray bands. The redshift estimate for GRB 200829A is $z = 1.29 \pm 0.04$. The results of the detection and analysis of the observations of the host galaxy follow next. We obtain estimates of the absorption parameters, the star formation rate, and the mass of the GRB 200829A host galaxy consistent with the parameters of other host galaxies of long GRBs. In the next section we present the results of our analysis of the chromatic inhomogeneity and the plateau on the light curve. Our estimates of the physical parameters are consistent with the model of a structured jet (Beniamini et al. 2020; Lamb et al. 2021; Duque et al. 2022) as a cause of the chromatic behavior. The plateau end time and the isotropic energy in the 0.3–10 keV band are in agreement with the correlation presented by Dainotti et al. (2008, 2021, 2022). In the final section we systematize the results of the observations and their analysis.

The luminosity distance D_L in this paper was calculated using the Λ CDM model of the Universe with the following cosmological parameters: $H_0 = 69.6 \pm 0.7$ km s $^{-1}$ Mpc $^{-1}$, $\Omega_m = 0.286 \pm 0.008$, and $\Omega_\Lambda = 0.714 \pm 0.008$ (Bennett et al. 2014). The statistical errors are given at the 1σ (66.7%) confidence level, unless stated otherwise.

2 OBSERVATIONS

2.1 Detection and the first observations

GRB 200829A was detected as a bright GRB of duration ~ 30 s with the BAT instrument onboard the Swift space

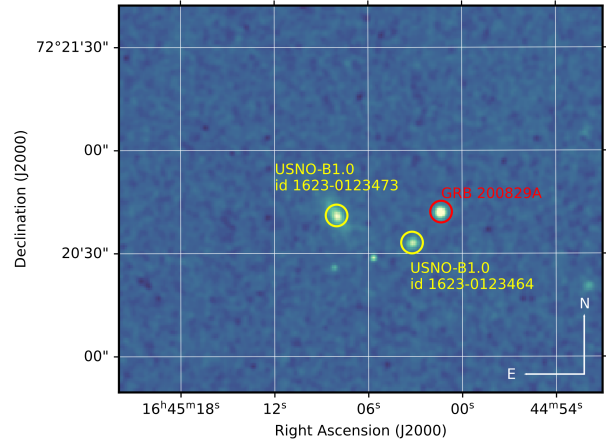


Figure 1. Image of the GRB 200829A (highlighted by the red circle) field taken with TShAO Zeiss-1000 on August 29, 2020, at 14:49:05 UT. The catalogued USNO-B1.0 objects are marked by the yellow circles and are labeled in the figure. In the image the north is upward and the east is leftward.

observatory; the report on its detection was distributed via the GCN/TAN¹ automated alert system (Siegel et al. 2020). The Swift observatory also detected an X-ray component of GRB 200829A with the XRT (0.3–10 keV). The X-ray source was found on August 29, 2020, at 14:01:43.1 UT, i.e., 128.7 s after the BAT trigger at 27'' from the center of the error circle for the gamma-ray component (Siegel et al. 2020; Goad et al. 2020).

The Swift Ultraviolet/Optical Telescope (UVOT) began to observe the GRB 200829A field almost immediately after the XRT. It detected a bright optical afterglow with a magnitude $white = 14.28 \pm 0.14$ (Siegel et al. 2020) at coordinates (J2000) R.A. = 16:44:49.14 and Dec. = +72:19:45.63 with a statistical error of $\pm 0.35''$ (90% confidence; Kuin et al. 2020). In the subsequent UVOT observations the source continued to fade (Kuin et al. 2020).

2.2 Ground observations

The ground-based optical observations of the fading afterglow of GRB 200829A began ~ 1 hr after the BAT trigger (Pozanenko et al. 2020) with the 1-meter Zeiss-1000 telescope of the Tien-Shan Astronomical Observatory (TShAO) as the part of GRB-IKI-FuN network (Volnova et al. 2021). One hour after the trigger the magnitude of the source was $R = 16.8 \pm 0.1$ in a single image (Fig.1) with an exposure time of 60 s.

The observations for 2.83 h, beginning from September 29, 2022, 14:49:05 UT, with the Zeiss-1000 telescope at TShAO allowed a detailed R-band light curve with a time resolution ~ 60 s to be constructed. Other instruments of the GRB-IKI-FuN network were additionally used to observe the fading afterglow. For example, the observations with the RC-36 telescope of the Kitab Observatory were carried out without a filter quasi-synchronously with TShAO. Beginning from August 29, 2020, 17:25 UT, telescopes on the Crimean Peninsula joined the observations: Zeiss-1000 at the observatory on Mount Koshka in the R and I filters, AZT-11 at the Crimean

¹ <https://gcn.nasa.gov>

Astrophysical Observatory (CrAO) in the R filter. Owing to the coordinated work of several telescopes, a detailed light curve was constructed over 12 h of observations. One day after the trigger the optical transient was observed with the AS-32 telescope of the Abastumani Astrophysical Observatory (AbAO) in the R filter and the Zeiss-1000 telescopes (Mount Koshka and the Special Astrophysical Observatory of the Russian Academy of Sciences (SAO RAS) in the R and I filters). Upper limits in the R filter were also obtained on the third and fifth days after the trigger in the observations with the AZT-33IK telescope at the Mondy observatory of the Institute of Solar-Terrestrial Physics, the Siberian Branch of the Russian Academy of Sciences. When the afterglow could no longer be observed with other telescopes due to the source brightness decline, $R \gtrsim 22^m.5$, the AZT-22 telescope of the Maidanak Astronomical Observatory (MAO) was used. MAO is located in a unique climatic region and, for this reason, the seeing (angular resolution) here reaches $0''.7$. A total of four deep upper limits were obtained in the R filter: three in the period from 13 to 45 days after the burst.

3 PROMPT EMISSION PHASE (GAMMA-RAYS)

3.1 GBM/Fermi data analysis

In our analysis of GRB 200829A we used the publicly accessible data of the GBM/Fermi experiment².

3.1.1 Light curve

The light curve in the energy range 7-850 keV constructed using data from the NaI04 and NaI08 detectors of the GBM/Fermi experiment most illuminated by the GRB 200829A source is presented in Fig.2.

The light curve can be arbitrarily divided into two activity episodes of approximately equal duration: the dim initial and main bright ones. The total duration of the gamma-ray emission from GRB 200829A in the GBM/Fermi experiment is more than 30 s, with the formal duration parameters $T_{90} = 8.4 \pm 0.1$ s and $T_{50} = 2.5 \pm 0.1$ s (Koshut et al. 1996) covering only the brightest part of the main episode. The values obtained characterize GRB 200829A as a long burst (type II, a collapsar) (see, e.g., Kouveliotou et al. 1993; Minaev et al. 2010b; Minaev & Pozanenko 2017).

As can be seen from Fig.2, both initial and main burst episodes have a complex structure that consists of a large number of overlapping pulses whose parameters, therefore, are impossible to reveal. Due to the superposition of pulses, analyzing the spectral evolution by the method of cross-correlation analysis for this burst is meaningless (see, e.g., Minaev et al. 2014).

3.1.2 Spectral analysis

To construct and fit the energy spectra, we used the RMfit v4.3.2 software package specially developed to analyze the GBM/Fermi data³. The technique of spectral analysis, including the choice of an optimal spectral model, is similar

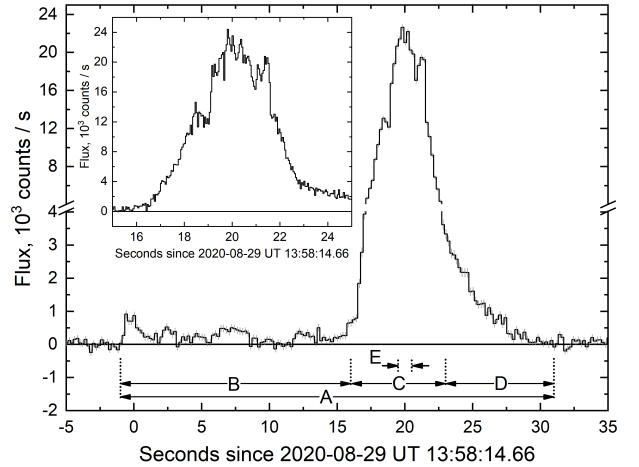


Figure 2. Light curve of GRB 200829A in the energy range 7–850 keV with a time resolution of 0.5 s (from GBM/Fermi data). The observed flux in counts per second over the background model is along the vertical axis; the time since the GBM/Fermi trigger in seconds is along the horizontal axis. The 1σ flux errors are shown. The vertical dotted lines mark the boundaries of the intervals used in our spectral analysis (see Table 1). The inset shows the light curve of the main episode with a time resolution of 0.05 s.

to that used in Gruber et al. (2014). We analyzed the energy spectra based on data from the most illuminated NaI_{04} , NaI_{08} , BGO_{00} , and BGO_{01} detectors.

We analyzed the energy spectrum of GRB 200829A in five different time intervals (Fig.2). Intervals A, B, C, D, and E correspond to the integrated spectrum of the event, the initial dim episode, the main part of the main episode, the decay stage of the main episode, and the peak in the light curve (the peak flux on a time scale of 1 s), respectively.

The energy spectrum of all the investigated components of GRB 200829A is unsatisfactorily described by both simple power-law model and thermal model; the optimal model is a power law with an exponential cutoff (CPL) or a broken power law (Band et al. 1993). The results of our spectral analysis (the parameters of the optimal spectral models) are presented in Table 1.

As an example, Fig.3 shows the integrated energy spectrum fitted by a broken power law (Band et al. 1993) with the parameter $E_p = 357 \pm 5$ keV characterizing the position of the peak in the energy spectrum νF_ν . The derived parameters of the energy spectrum for all the investigated components of the light curve are typical for GRBs (see, e.g., Gruber et al. 2014). It can be seen from Fig. 3 that the scatter of data points relative to the model is fairly large. This is apparently due to the systematic effects (for example, inaccurate response matrices and detector cross-calibration) that arise when reconstructing the photon spectrum with the RMfit v4.3.2 software package.

3.1.3 $E_{p,i} - E_{iso}$ correlation

GRBs are characterized by a number of correlations between various observed parameters. One of the best-known ones is the correlation of the isotropic equivalent energy released in the energy range 1 keV – 10 MeV, E_{iso} , with the position of the extremum in the energy spectrum νF_ν in the source

² <ftp://legacy.gsfc.nasa.gov/fermi/data/>

³ <http://fermi.gsfc.nasa.gov/ssc/data/analysis/rmfit/>

[t]

Table 1. Results of our spectral analysis of GRB 200829A in the gamma-ray band based on GBM/Fermi data

Interval ^a (c)	Spectral model ^b	α	β	E_p ^c (keV)	Fluence ^d (10^{-5} erg cm ⁻²)	E_{iso} ^e (10^{53} erg)	EH ^f
A = -1 - 31	Band	-0.552 ± 0.014	-2.468 ± 0.026	357 ± 5	22.17 ± 0.08	13.02 ± 0.13	0.45
B = -1 - 16	CPL	-1.23 ± 0.10	—	249 ± 37	0.68 ± 0.04	0.323 ± 0.025	1.42
C = 16 - 23	Band	-0.392 ± 0.013	-2.477 ± 0.016	363 ± 4	20.55 ± 0.06	12.16 ± 0.08	0.47
D = 23 - 31	Band	-0.89 ± 0.10	-2.30 ± 0.09	136 ± 13	1.189 ± 0.026	0.66 ± 0.04	0.57
E = 19.5 - 20.5	Band	-0.333 ± 0.023	-2.288 ± 0.020	393 ± 8	6.011 ± 0.033	3.88 ± 0.04	0.79

^a The time interval relative to the GBM/Fermi trigger.

^b CPL is a power law with an exponential cutoff, Band is a broken power law (Band et al. 1993).

^c The peak energy in the energy spectrum $\nu F\nu$.

^d The fluence in the range 10 - 1000 keV in the observer frame.

^e The isotropic equivalent energy in the range 1 keV - 10 MeV in the source frame ($z = 1.29 \pm 0.04$, see below).

^f The classification parameter EH (Eq 2).

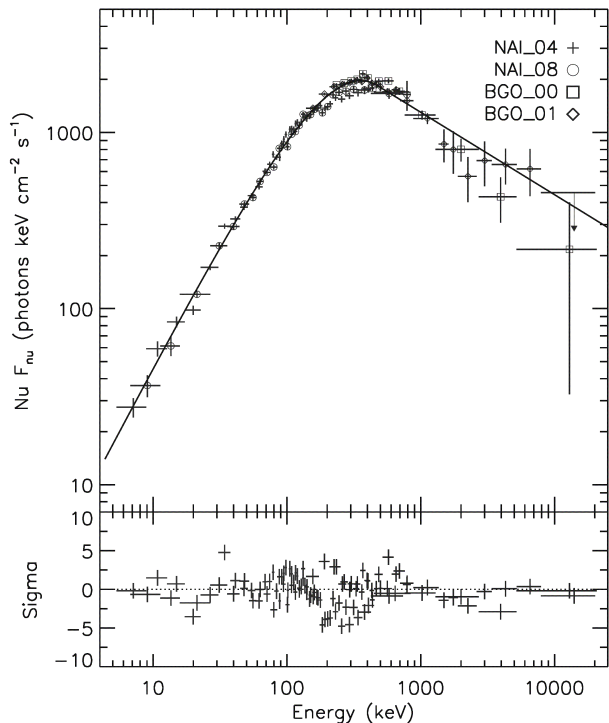


Figure 3. The energy spectrum $\nu F\nu$ of GRB 200829A constructed using data from the NaI_{04} , NaI_{08} , BGO_{00} , and BGO_{01} detectors of the GBM/Fermi experiment in the time interval A = -1 - 31 s relative to the trigger covering the GRB prompt phase (the upper part of the figure). The smooth curve indicates a broken power-law spectral fit (Band et al. 1993). The deviation of the spectral model from the experimental data expressed in standard deviations is shown in the lower part.

frame, $E_{p,i}$ (Amati et al. 2002). The nature of the correlation is still the subject of discussion. One possible explanation implies viewing angle effects: the smaller the angle between the source-observer line and the jet axis, the brighter and spectrally harder the GRB (Eichler & Levinson 2004; Levinson & Eichler 2005; Pozanenko et al. 2018). The parameter E_{iso} is calculated from Eq. (1), where F is the fluence (time-integrated flux) in the energy range 1 keV - 10 MeV in the source frame, D_L is the luminosity distance to the source, and z is its redshift. The corresponding values of the parameter E_{iso} for GRB 200829A were calculated using the redshift $z = 1.29 \pm 0.04$ and are given in Table 1. To estimate

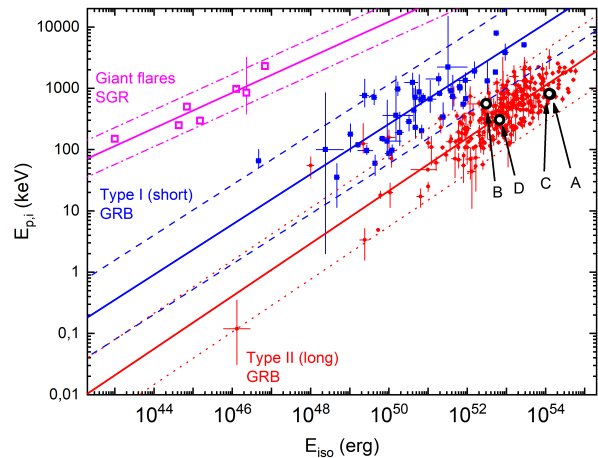


Figure 4. $E_{p,i} - E_{iso}$ diagram for type I (blue squares) and type II (red circles) GRBs and SGR giant flares (magenta unfilled squares) with the corresponding fits (solid lines) and 2σ correlation regions (dashed lines). The black unfilled circles indicate the positions of GRB 200829A and its individual episodes (see Table 1).

the fluence in the energy range 1 keV - 10 MeV, we used an extrapolation of the spectral model to low energies (below 6 keV in the observer frame),

$$E_{iso} = \frac{4\pi D_L^2 F}{1+z}. \quad (1)$$

Fig. 4 presents a $E_{p,i} - E_{iso}$ diagram for one of the most complete samples of 317 GRBs with known redshifts and determined parameters $E_{p,i}$ published in Minaev & Pozanenko (2020b, 2021) and for 7 giant flares from soft gamma repeaters (SGRs), for which the $E_{p,i} - E_{iso}$ correlation was first found by Minaev & Pozanenko (2020a).

On the $E_{p,i} - E_{iso}$ diagram GRB 200829A occupies a position typical for long (type II) GRBs, while being one of the brightest bursts with $E_{iso} > 10^{54}$ erg. The individual burst episodes are also located in the correlation region of long GRBs.

3.1.4 $T_{90,i} - EH$ diagram

The $E_{p,i} - E_{iso}$ correlation can also be used for the classification of GRBs, since the correlation region of type I (short) GRBs is above the correlation region of type II (long) GRBs,

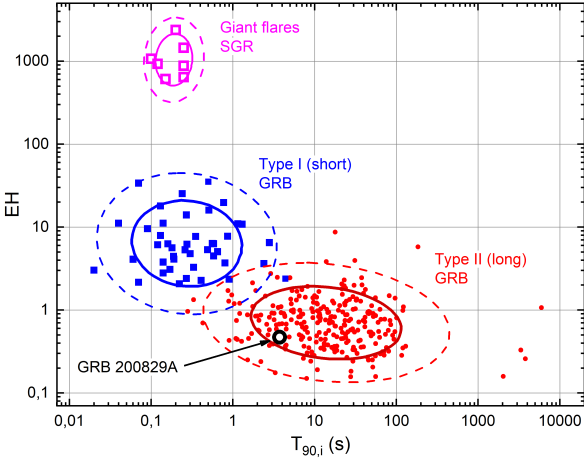


Figure 5. $T_{90,i} - EH$ diagram for type I (blue squares), type II (red circles) GRBs, and giant SGR flares (pink open squares) with the corresponding results of a cluster analysis (the 1σ and 2σ cluster regions are indicated by the thick solid and thin dashed curves, respectively). The black unfilled circle indicates the position of GRB 200829A.

with the correlation for both types of GRBs being described by a power law with a single index, $\alpha = -0.4$ (Minaev & Pozanenko 2020a,b). For this purpose, Minaev & Pozanenko (2020b) introduced the parameter EH (Eq. 2) that characterizes the GRB position on the $E_{p,i} - E_{iso}$ diagram. Compared to type II GRBs, type I GRBs have a greater spectral hardness $E_{p,i}$ at a lower total energy E_{iso} and, as a consequence, a larger value of the parameter EH :

$$EH = \frac{(E_{p,i}/100 \text{ keV})}{(E_{iso}/10^{51} \text{ erg})^{0.4}}. \quad (2)$$

The most efficient GRB classification method suggests a joint analysis of the parameter EH and the duration parameter $T_{90,i}$ measured in the source frame (Minaev & Pozanenko 2020a,b, 2021). Fig.5 presents a $T_{90,i} - EH$ diagram for 317 GRBs and 7 giant SGR flares from Minaev & Pozanenko (2020a,b, 2021) that provides the best separation into clusters of the corresponding types of transients (the smallest overlap region) among the known classification schemes.

GRB 200829A being investigated is located within the 1σ cluster region of type II (long) GRBs, although it has a relatively small value of the duration parameter, $T_{90,i} = 3.7$ s, corresponding to the overlap region of the duration distributions for the classes of long and short bursts, emphasizing the stability of the classification system based on the $T_{90,i} - EH$ diagram method. The values of the parameter EH for GRB 200829A and its individual episodes are given in Table 1.

3.2 BAT/Swift Data Analysis

As has been shown above, GRB 200829A is characterized by a fairly hard energy spectrum with $E_p > 350$ keV located outside the effective BAT/Swift sensitivity range, 15 – 150 keV. Therefore, in this section devoted to analyzing the burst based on BAT/Swift data, we restricted our study only to its light curve.

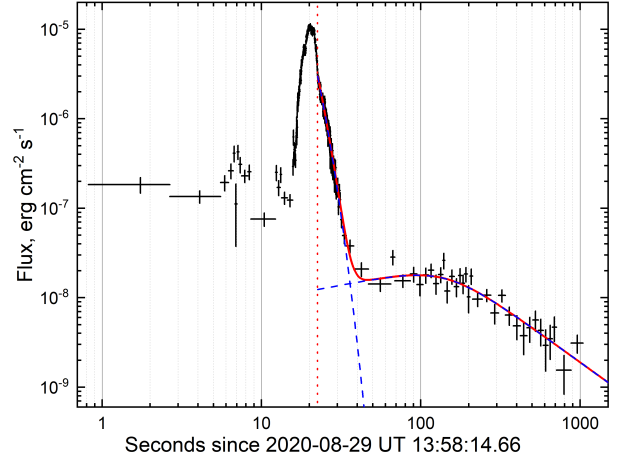


Figure 6. Light curve of GRB 200829A in the 15 – 50 keV energy band (from BAT/Swift data). The energy flux in $\text{erg cm}^{-2} \text{s}^{-1}$ is along the vertical axis; the time since the GBM/Fermi trigger in seconds is along the horizontal axis. The 1σ flux errors are shown. The light curve is fitted by the sum of an exponential model and a broken power law (blue dashed lines). The red solid line is their sum; the vertical red dotted straight line marks the beginning of the time interval in which the fit was constructed.

As the data source we used the publicly accessible service⁴. Although the trigger time in the BAT/Swift experiment differs by 79.74 s from that in GBM/Fermi, as the trigger time T_0 we will use the trigger time of the latter, since it corresponds more closely to the start time of the burst prompt phase (Fig.2).

The light curve constructed in the 15 – 50 keV energy band is presented in Fig.6. After binning the light curve by the signal accumulation method until a certain statistical significance was reached, we detected a weak, but statistically significant extended emission with a duration ~ 1000 s that is a separate component of the light curve.

The light curves of individual pulses at the prompt phase of GRBs are usually characterized by the so-called FRED shape (fast rise – exponential decay, see, e.g., Norris et al. 2005; Hakkila & Preece 2011; Minaev et al. 2014). The light curve of GRB 200829A has a complex shape and is a superposition of several significantly overlapping FRED pulses, making it difficult to fit the light curve of the entire prompt phase. Therefore, when jointly fitting the component of the prompt phase and the extended emission, we used only the decay stage of the last pulse of the prompt phase that was described by an exponential model.

The light curve of the extended emission is characterized by an initial quasi-plateau stage followed by a power-law flux decline. To describe this component of the light curve, we used a broken power law (Beuermann et al. 1999).

The results of jointly fitting the decay stage of the prompt phase and the extended emission component by the above models are presented in Fig.6. At the initial stage the index of the light curve for the extended emission is $\alpha = 0.34 \pm 0.27$, which does not rule out the plateau stage ($\alpha = 0$), the break in the light curve is observed at $t_{br} = 143 \pm 38$ s, and the index after the break is $\beta = -1.28 \pm 0.18$. The index after

⁴ https://www.swift.ac.uk/burst_analyser/

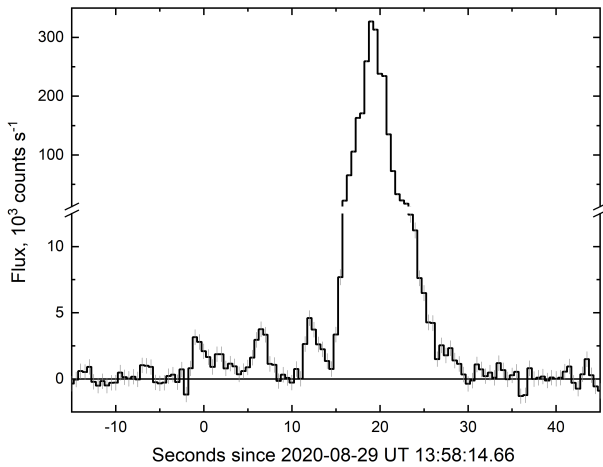


Figure 7. Light curve of GRB 200829A at energies above 80 keV with a time resolution of 0.5 s (from SPI-ACS/INTEGRAL data). The observed flux in counts per second over the background model is along the vertical axis; the time since the GBM/Fermi trigger in seconds is along the horizontal axis. The 1σ flux errors are shown.

the break is close to a value typical for an afterglow ($\beta \sim -1$), suggesting a connection of the extended emission component with the afterglow, which is typical for bright GRBs (see, e.g., Mozgunov et al. 2021). In our further analysis of the X-ray and optical data this interpretation will be confirmed.

3.3 SPI-ACS/INTEGRAL Data Analysis

GRB 200829A was also detected by the anticoincidence shield (ACS) of the SPI gamma-ray spectrometer onboard the INTEGRAL observatory (von Kienlin et al. 2003).

The light curve of GRB 200829A at energies above 80 keV with a time resolution of 0.5 s constructed from the SPI-ACS/INTEGRAL data⁵ is presented in Fig. 7. Despite the stable back-ground conditions in the time interval from -5000 to 5000 s around the GRB typical for the SPI-ACS detector (Minaev et al. 2010a; Mozgunov et al. 2021), no extended emission was detected by SPI-ACS/INTEGRAL, although it was recorded in the BAT/Swift experiment with great confidence.

This is probably due to the relatively soft energy spectrum (the small fraction of high-energy emission) of this component and the high lower sensitivity threshold of the ACS detector (80 keV). A possible precursor (Minaev & Pozanenko 2017) was not detected either. Although several dim episodes with a total duration of about 15 s, from which the burst prompt phase begins, were recorded in the SPI-ACS experiment (Fig. 7), the duration parameters T_{90} and T_{50} cover only the main bright episode and are $T_{90} = 5.5 \pm 0.1$ s and $T_{50} = 2.1 \pm 0.1$ s, confirming the classification of this burst as type II (long).

According to the SPI-ACS/INTEGRAL data, the time-integrated flux from GRB 200829A was $F = (115.3 \pm 0.3) \times 10^4$ counts. Using the cross-calibration of the SPI-ACS and GBM experiments for GRBs from Pozanenko et al. 2020, we

obtain an estimate of the fluence in the energy range 10 – 1000 keV, $F \gtrsim 2.9 \times 10^{-4}$ erg cm⁻².

Given the systematic calibration error for the SPI-ACS response to GRB energy spectra differing in shape, the estimated fluence can vary within the range $8.4 \times 10^5 - 9.8 \times 10^{-4}$ erg cm⁻² (at 2σ confidence). The estimated fluence agrees well with the value obtained through our spectral analysis of the GBM/Fermi data (Table 1).

4 AFTERGLOW

In our analysis we used the public Swift Burst Analyzer⁶ data (Evans et al. 2007, 2009) from the BAT, XRT, and UVOT experiments onboard Swift to construct the gamma-ray, X-ray, and optical light curves, respectively. We also used the public observational data accessible via the GCN/TAN service⁷: the observations with the RC80 robotic telescope at the Konkoly Observatory (Vinko et al. 2020) in the r' , and i' filters, the observations with the Zeiss-1000 SAO RAS telescope in the R_c and I_c filters, the observations with the NEXT telescope (Zhu et al. 2020a,b) and the observations with the Liverpool telescope (Izzo 2020) in the g' , r' , i' , and z' filters. The publicly available images from the Nordic Optical Telescope (NOT) in the r' filter were retrieved from the NOT FITS Header Archive⁸. The light curves were fitted using the `lmfit`⁹ package (Newville et al. 2021) for python.

4.1 Analysis of the optical observations

The afterglow of GRB 200829A was observed for the first ~ 3 days in the X-ray and optical bands. To construct the optical light curve of the GRB 200829A afterglow, we processed the GRB-IKI-FuN observational data and the publicly accessible Nordic Optical Telescope (NOT) data using the developed software pipeline (Pankov et al. 2022) based on the APEX package (Kouprianov 2012; Devyatkin et al. 2010). The standard data processing procedure includes the calibration and quality control of the original images, their alignment and stacking (if required), the extraction of objects in the images, the astrometry and photometry, the construction of a local catalog, the search for and identification of transients in it. In addition to the software pipeline (Pankov et al. 2020), we used the PyRAF software package (Science Software Branch at STScI 2012) in individual cases, for example, when an optical transient had a low signal-to-noise ratio, $S/N < 5$. We performed the astrometry of images based on the USNO-B1.0 reference catalog (Monet et al. 2003). The photometric calibration stars were chosen by cross-matching the stars from USNO-B1.0 with the PanSTARRS PS1 catalog (Chambers et al. 2016). This allowed us to calibrate the source magnitudes in the images taken both in R , I , and in r using the same stars. The photometry of images without a filter was performed relative to the R magnitude. A log of optical observations is given in Appendix A. Figure 8 presents a multicolor optical light curve; for clarity, the magnitudes in

⁵ <http://isdc.unige.ch/~savchenk/spiacs-online/spiacs-ipnlc.pl>

⁶ https://www.swift.ac.uk/burst_analyser/00993768

⁷ <https://gcn.gsfc.nasa.gov/other/200829A.gcn3>

⁸ <http://www.not.iac.es/observing/forms/fitsarchive/>

⁹ <https://github.com/lmfit/lmfit-py>

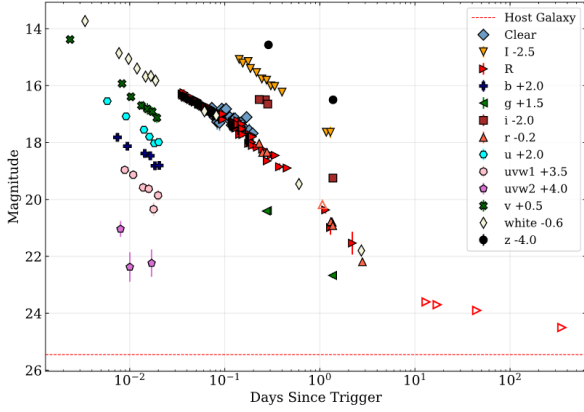


Figure 8. Multicolor optical light curve of GRB 200829A. The time since the GBM trigger (days) is along the horizontal axis, and the apparent magnitude is along the vertical axis. The symbols designate the photometric magnitudes obtained in various filters. The dashed line indicates the brightness level of the GRB 200829A host galaxy. The unfilled symbols designate the upper limits (at 3σ confidence level).

all filters, except R , were separated relative to their initial values.

A break in the R filter, which may be related to the geometrical viewing angle effect typical for relativistic jets (Sari et al. 1999; Piran 2004), is traceable in Fig. 8. The magnitudes in the light curve were not corrected for the Galactic extinction characterized by the color excess $E(B - V) = 0.0364$ (Schlegel et al. 1998) toward GRB 200829A. Since it is impossible to establish the spectral evolution at the entire optical afterglow stage due to insufficient quasisynchronous coverage in different filters, we assume its absence. Under this assumption the light curves in the g , r , i , z , I , u , b , v , $uvw1$, $uvw2$ filters and in *clear* and *white* light were reduced to the R light curve (the data are presented predominantly in this filter) by additionally multiplying the flux by the appropriate numerical coefficient at which the best agreement with the data from the χ^2 test is achieved. In our subsequent analysis of the afterglow we will consider this monochromatic optical light curve.

4.2 Analysis of the X-ray observations

The X-ray afterglow was also observed quasisynchronously with the optical one by the XRT/Swift instrument (Burrows et al. 2005a). The XRT is a Wolter I telescope with a focal length of $EFF = 3500$ mm and a $FOV = 23.6' \times 23.6'$. An E2V CCD detector with 600×600 pixels and cooled to -100 °C was mounted at the focal plane. As a result, an angular resolution of $\theta \sim 3''$ is achieved. The telescope operates in the 0.3 – 10 keV energy band in several modes, among which are Windowed Timing (WT), and Photon Counting (PC). In the WT mode a good time resolution (~ 1.8 ms) is achieved, but, at the cost of, the angular and spectral resolutions. In the PC mode the signal readout rate from the CCD is reduced to ~ 2.5 s, but other characteristics do not change. The WT and

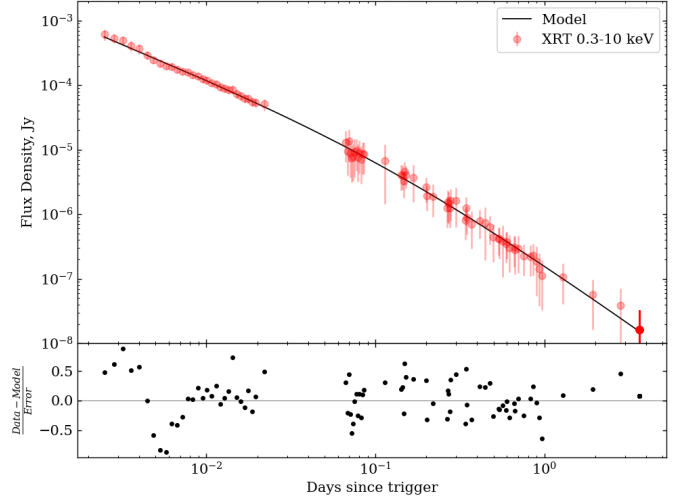


Figure 9. The upper panel shows the X-ray light curve of GRB 200829A. The time since the GBM trigger in days is along the horizontal axis, while the observed flux density in Jy is along the vertical axis. The circles designate the values, while the thick solid line indicates the broken power law fit. The lower panel shows the deviation of the experimental flux densities from the fit in standard deviations σ .

PC modes are used at fluxes $F_X = 1 - 600$, and $F_X < 1$ mCrab, respectively (Burrows et al. 2005a).

The X-ray light curve of GRB 200829A was constructed from the data publicly available via the **Swift Burst Analyzer**¹⁰ service. The data contain the results of observations (time and flux) in the WT and PC modes and span a period ~ 2 days. The observed X-ray flux was grouped into bins whose duration increases on a logarithmic scale, starting from 60 s. The Galactic extinction on the line of sight was not taken into account. Thus, the light curve was smoothed, while the significance of individual measurements was improved. Fig. 9 presents the X-ray light curve of the GRB 200829A afterglow.

According to Fig. 9, a break is traceable in the X-ray light curve, as in the optical one. Fitting the light curve by the Beuermann function (Beuermann et al. 1999) allowed us to determine the slope of the light curve and the position of the break on the time scale. For example, the slope is $\alpha_1 = 1.06 \pm 0.03$ before the break and $\alpha_2 = 1.88 \pm 0.06$ after the break. Note that the slope for the X-ray afterglow $\alpha_1 = 1.06 \pm 0.03$ before the break agrees well with the slope for the extended emission in the soft 15 – 50 keV gamma-ray band $\beta = 1.28 \pm 0.18$ found previously. Hence a correlation of the observed extended emission and the afterglow can be assumed. According to this assumption, the gamma-ray light curve was rescaled to the X-ray light curve in the time interval 100 – 1000 s relative to T_0 (in which the data from both telescopes were obtained) assuming the afterglow to be achromatic in the X-ray and soft gamma-ray bands. According to the χ^2 test, the conversion coefficient is $k = F_{XRT}/F_{BAT} = 4.54$. Thus, we constructed the most

¹⁰ https://www.swift.ac.uk/burst_analyser/00993768/

complete light curve of the X-ray afterglow that will be used in our further analysis.

4.3 Multiwavelength light curve

Let us investigate the previously constructed X-ray and optical light curves (presented together in Fig. 10) and fit and interpret them.

In Fig. 10 both X-ray and optical light curves consist of three episodes (not counting the burst prompt phase): a flare gradually decays into a power-law flux decline and then a break after which the flux fades according to a steeper law. At the same time, the leading edge of the flash looks rather steep against the background of the power-law decay. Since in the optical light curve the time of the peak cannot be unambiguously determined due to the absence of data, we assume that it coincides with that for the X-ray band.

To fit the light curves, we chose a function in the form of a sum of two power laws with a smooth break (Beuermann et al. 1999) defined by Eq.3:

$$F(t) = (F_1^{-n} + F_2^{-n})^{-\frac{1}{n}} + (F_3^{-n} + F_4^{-n})^{-\frac{1}{n}} \quad (3)$$

where, $F_i = (\frac{t-T_0}{t_{b_i}})^{\alpha_i}$, t – the time since trigger (days), t_{b_i} – the break time (days), α_i – are the indices before and after the break, n – the smoothing parameter ($n > 0$), $i = 1, 2, 3, 4$, $j = 1$ at $i = 1, 2$, and $j = 2$ at $i = 3, 4$. The fitting results are presented in the Table 2; the values marked by * were fixed. The fitting by the two-component model was performed in the intervals ~ 50 s – 3.66 days in the X-ray band and 283 s – 2.80 days in the optical band (relative to the GBM/Fermi trigger). Fig.10 (bottom) demonstrates the color evolution between the X-ray and optical bands.

4.4 Redshift estimation

To estimate the redshift, we used the technique of simultaneously fitting the spectral energy distribution in the optical and X-ray bands under absorption conditions (Schady et al. 2010). The time-sliced XRT X-ray spectrum and the UVOT optical images were retrieved via the Swift Burst Analyser service. The spectra span the time interval 1554 – 1638 s relative to T_0 , where no significant color evolution is observed. The data were processed with the HEASOFT¹¹ (Blackburn 1995) software package. Figure 11 presents a multiwavelength spectrum of the GRB 200829A afterglow fitted by the model curve (see below).

As the spectral model we use a power law and a broken power law. The model takes into account the optical extinction by interstellar dust grains and the photoelectric X-ray absorption and is represented by Eq. (4) in terms of XSPEC (HEASOFT), where the `zdustr` components are responsible for the optical extinction.

$$F = \text{zdustr} \times \text{zdustr} \times \text{phabs} \times \text{zphabs} \times \text{powerlaw} \quad (4)$$

These components are based on an empirical dust extinction law (Pei 1992). Three extinction laws are available in

XSPEC: the Milky Way (MW), the Large Magellanic Cloud (LMC), and the Small Magellanic Cloud (SMC). The extinction model is characterized by the color excess $E(B-V)$, the total-to-selective extinction ratio $R(V) = A(V)/E(B-V)$, where $A(V)$ is the extinction, and the redshift z . The `phabs` and `zphabs` components allow the absorption by hydrogen in the Galaxy and the burst host galaxy to be taken into account. Both components are defined by the column density N_H in units of 10^{-22} cm⁻², while `zphabs` is also defined by the redshift z . The `powerlaw` component is responsible for the power law spectrum and is specified by the spectral index β and the normalization K (photons⁻¹ keV⁻¹ cm⁻² at 1 keV). During our fitting the Galactic extinction parameters were fixed: $E(B-V) = 0.0364$ (Schlegel et al. 1998), $R(V) = 3.08$ (Pei 1992), $A(V) = R(V)E(B-V) = 0.20$, and $N_H = 0.039 \times 10^{-22}$ cm⁻² (HI4PI Collaboration et al. 2016). The redshift of the Galaxy was also fixed ($z = 0$). We found that the spectral data cannot be fitted with the broken power law and, therefore, this model was not considered. Table 3 presents the results of fitting the spectral data for the early afterglow of GRB 200829A by the model defined in Eq. (4). The best spectral fit from the standpoint of the $\chi^2/d.f.$ test is achieved when choosing the MW extinction law for the GRB host galaxy (see Table 3). The estimate of the photometric redshift $z = 1.29 \pm 0.04$ consistent with the independent estimate of $z = 1.25 \pm 0.02$ obtained previously by Oates et al. (2020) by the same method corresponds to it. However, in contrast to Oates et al. (2020), we also provide our estimates of the extinction parameters in the burst host galaxy. Note that in both cases the error is statistical. Below, $z = 1.29 \pm 0.04$ will be deemed to be the redshift of GRB 200829A.

5 HOST GALAXY

We detected the host galaxy of GRB 200829A and calculated its contribution to the optical light curve using the observation with the Big Telescope Azimuthal (BTA) at SAO RAS ~ 2 years after the GRB. The BTA observation was carried out on July 31, 2022, at 18:30 UT with SCORPIO-1 (with a E2V CCD42-40 array) in the R filter. A host galaxy candidate, whose coordinates coincided with those of GRB 200829A within the $\pm 0.1''$ error limits and whose brightness uncorrected for the Galactic extinction was $R = 25.5_{-0.3}^{+0.4}$, was found in the image with a total exposure time of 2910 s. Figure 12 presents a fragment of the image in which the host galaxy candidate is marked.

The apparent magnitude after its correction for the Galactic extinction $A_R = 0.083$ (Schlafly & Finkbeiner 2011) is $R = 25.4_{-0.3}^{+0.4}$. This magnitude is consistent with the magnitude of a sample of host galaxies for $z = 1.29$ (see, e.g., Pozanenko et al. 2008). The absolute magnitude of the host galaxy is $M_R \sim -19.44$ for $z = 1.29$. Let us estimate the star formation rate (SFR) and the host mass M_{host} from the relation $\log SFR = -0.381M_r - 8.029 \pm 0.486 M_\odot \text{ yr}^{-1}$, where M_r is the absolute r magnitude of a spiral galaxy (see, e.g., Mahajan et al. 2018). The absolute magnitude of the GRB 200829A host galaxy will be $M_r = -19.20$, given the conversion of the magnitude from R to r ($r = R + 0.21$), and the correction for the Galactic extinction $A_r = 0.088$ (Schlafly & Finkbeiner 2011). The SFR estimate will then be $\log SFR \approx$

¹¹ <https://heasarc.gsfc.nasa.gov/ftools>

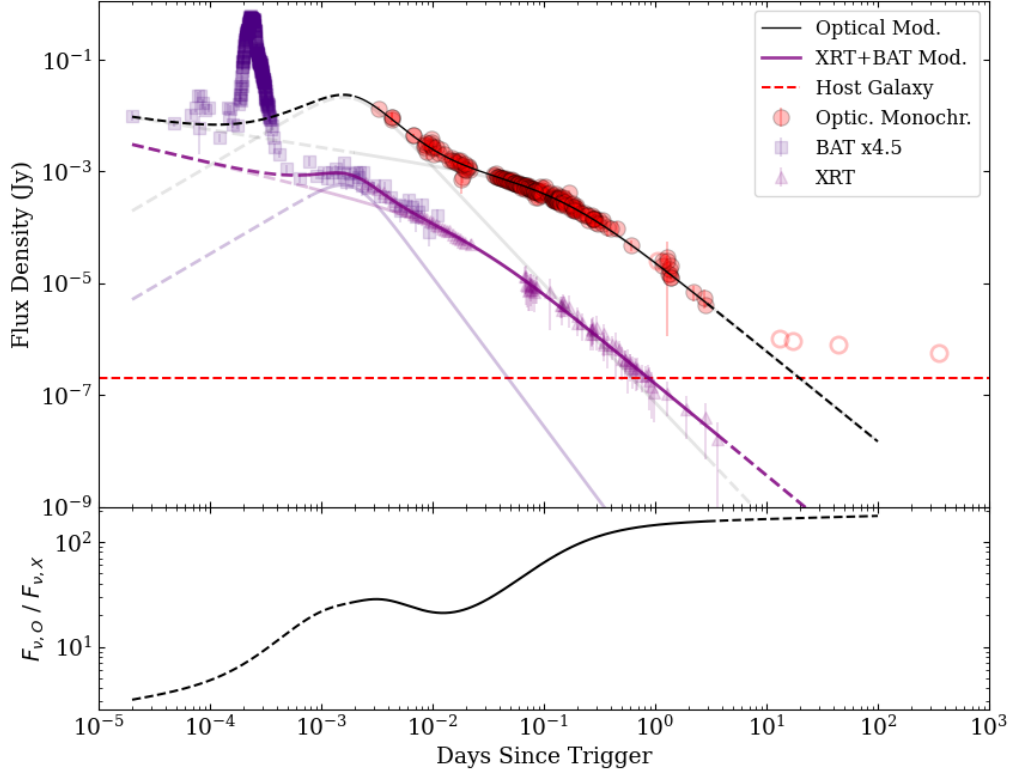


Figure 10. The upper panel shows the light curve of GRB 200829A. The time since the GBM trigger $t - T_0$ (days) is along the horizontal axis, while the spectral flux density (Jy) is along the vertical axis. The photometric values in the optical filters (red filled squares) were combined into a single monochromatic curve. The X-ray light curve (violet filled triangles) was combined with the gamma-ray one (dark-blue filled squares) assuming that the extended emission corresponds to the X-ray afterglow. The open symbols designate the upper limits. The model curves are marked by the solid lines. The lower panel shows a graph of the evolution of the optical-to-X-ray flux ratio.

Table 2. Afterglow fitting results

Range	F_1 mJy	α_1	α_2	t_{b1} $\times 10^{-3}$ day	F_2 mJy	α_3	α_4	t_{b1} day	n	$\chi^2 / d.f.$
X-ray	0.52 ± 0.10	-1.2 ± 1.0	2.7 ± 0.5	1.9 ± 0.4	0.06 ± 0.03	0.5 ± 0.2	1.6 ± 0.1	0.02 ± 0.01	1*	0.34
Optical	10 ± 3	-1.2^*	1.9 ± 0.2	1.9^*	0.27 ± 0.04	0.3 ± 0.1	1.64 ± 0.08	0.15 ± 0.03	1*	1.1

Table 3. Results of fitting the multiwavelength spectrum of the early afterglow.

Extinction law	$E(B - V)$ mag	$R(V)$	$A(V)$ mag	z	nH 10^{22} cm^{-2}	β	$\chi^2 / d.f.$
MW	0.36 ± 0.02	3.08*	1.11 ± 0.02	1.29 ± 0.04	0.26 ± 0.03	1.72 ± 0.02	248/236
LMC	0.31 ± 0.21	3.16*	0.98 ± 0.21	0.40 ± 0.75	0.42 ± 0.59	1.56 ± 0.01	329/236
SMC	0.19 ± 0.04	2.93*	0.56 ± 0.04	1.36 ± 0.33	0.17 ± 0.06	1.60 ± 0.02	316/236

The values of $E(B - V)$, $R(V)$, $A(V)$, and N_H are given for the host galaxy, and the corresponding values for the Galaxy were fixed: $E(B - V) = 0.0364$ mag, $R(V) = 3.08$, $A(V) = 0.20$ mag, and $N_H = 0.039 \times 10^{22} \text{ cm}^{-2}$. The values of the fixed parameters are denoted with "*" symbol.

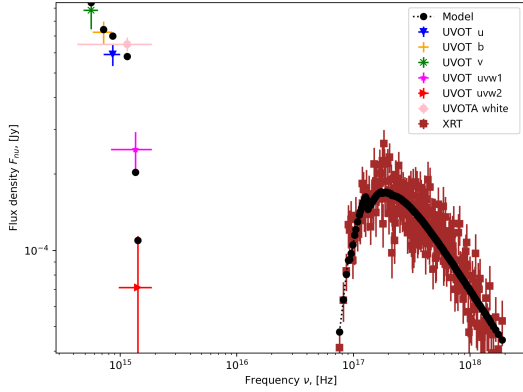


Figure 11. Spectrum of GRB 200829A in the interval 1554 – 1638 s relative to T_0 . The emission frequency (Hz) is along the horizontal axis, while flux (Jy) is along the vertical axis. The model is designated by the black circles, while the remaining symbols mark the data.

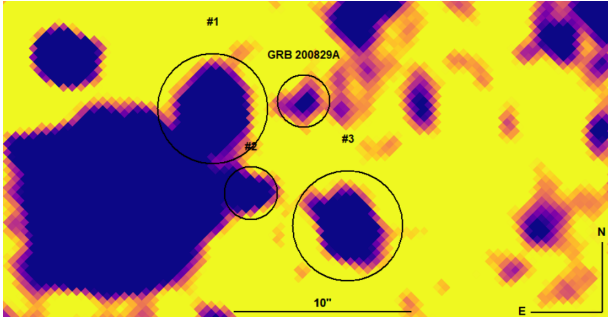


Figure 12. Fragment of the R -band image of the GRB 200829A field obtained with the BTA telescope at SAO RAS. A diffuse object, the host galaxy, is seen at the location of the transient.

$-0.715 \pm 0.486 M_{\odot} \text{ yr}^{-1}$, whence we can estimate the host mass as $SFR \times T_{age}$, where T_{age} is the host age. We obtain an estimate of the host mass $M_{host} \sim 8.5 \times 10^9 M_{\odot}$. For comparison, the absolute magnitude of the GRB 181201A host galaxy is $M_R = -18.5 \pm 0.2$, while its mass is $\sim 1.2 \times 10^9 M_{\odot}$ (Belkin et al. 2020) (from the results of modelling the galaxy spectrum).

The previously obtained spectral fitting results (see Table 3) also allow one to determine the ratio $N_H/A(V)$, from which the similarity of dust properties in various galaxies to be judged. If the dust properties are the same in the Universe, then the ratio $N_H/A(V)$ must increase linearly with distance to the galaxy. For example, for the host galaxy of GRB 200829A $N_H/A(V) \approx 2.4 \times 10^{22} \text{ cm}^{-2}$. The column density-to-extinction ratio for the host galaxy of GRB 200829A is consistent with most host galaxies of other GRBs represented in the sample (Covino et al. 2013), for which $N_H/A(V) \approx 1.6 \times 10^{21} \text{ cm}^{-2}$, as is clearly shown in Fig. 13.

6 POSSIBLE SN

The long GRB 200829A could be accompanied by an SN. The SN search campaign was undertaken at the AZT-22 MAO

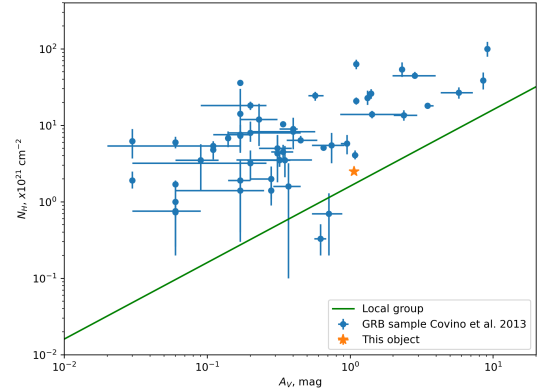


Figure 13. Plot of the $N_H - A(V)$ relation. The blue squares mark the values from the GRB host galaxies (Covino et al. 2013), while the green line marks the linear law $\log(y) = 1.6 \log(x)$ that the overwhelming majority of galaxies in the sample match. The red star designates $N_H - A(V)$ for the GRB 200829A host galaxy.

telescope in the period 10 – 46 days after the GRB detection. This period corresponds to a typical SN peak (8 – 40 days) in the source frame (see, e.g. Belkin et al. 2020). During the observations the upper limit was $R = 24.0$ (3σ); however, no SN was detected. The upper limit for the absolute magnitude of a possible SN at $z = 1.29$ is $M_R > -23.0$. Here we made a correction for the extinction in the Galaxy $A_{R,MW} = 0.083$ and the GRB host galaxy $A_{\lambda} = 2.14 \pm 0.04$, where $\lambda = 0.641 \times (1+z) \mu\text{m}$ is the effective wavelength of the R filter at redshift z . A_{λ} was calculated from the following formula Eq.(5):

$$A_V \simeq \frac{E(B - R)}{\xi\left(\frac{\lambda_B}{1+z}\right)\xi\left(\frac{\lambda_R}{1+z}\right)} \quad (5)$$

where, $E(B - R)$ – is the color index between the B and R filters, ξ – is the extinction law, λ_B and λ_R , effective wavelengths of the filters B , and R , respectively.

Our estimate is consistent with the absolute magnitude distribution of SNe from GRBs (Belkin et al. 2020).

7 DISCUSSION

7.1 Chromatic behavior of the light curve

The multiwavelength light curve (Fig. 10) of GRB 200829A has an asynchronous (chromatic) behavior in the early afterglow that encompasses the irregularity (flare) and continues up until the jet break. The chromaticity during the flare can be interpreted in terms of the model of a structured jet (see, e.g., Duque et al. 2022). According to this model, harder emission is observed closer to the jet axis and, for this reason, the X-ray emission corresponds to the part of the jet that is characterized by a larger gamma factor. Let us estimate the gamma factor of the jet from the following formula (see, e.g., Han et al. 2022):

$$\Gamma_0 = 2 \left[\frac{3E_{\gamma}(1+z)^3}{32\pi n m_p c^5 \eta t_p^3} \right]^{1/8} \quad (6)$$

where, m_p – is the proton mass, c – is the speed of light, $E_\gamma = 2\pi(1 - \cos\theta_j)E_{iso}$ – is the gamma-ray energy of the jet corrected for its opening angle θ_j , $\eta = E_\gamma/\xi E_{iso}$, $t_p = t_b - \alpha_1/\alpha_2)^{1/\omega(\alpha_2 - \alpha_1)}$, t_b – is the break time relative to T_0 (days), α_1 , α_2 – are the power-law slopes of the light curve before and after the break, respectively, and $\omega = 1$. Note that in the light curve the jet break cannot be unambiguously determined. Therefore, we will choose t_b from Table 2 in such a way that the open angle is not an extreme one. For example,

(i) $t_b = T_0 + 1.9 \times 10^{-3}$ days corresponds to the flare peak in the early afterglow,

(ii) $t_b = T_0 + 0.02$ days corresponds to the break of the second component in the X-ray band,

(iii) $t_b = T_0 + 0.15$ days corresponds to the break of the second component in the optical band.

The opening angle of the jet cone can be determined from the formula given below (e.g. Sari et al. 1999; Zhang et al. 2007):

$$\theta_j \sim 0.161 \left(\frac{t_b}{1+z} \right)^{3/8} \left(\frac{\xi E_{52}}{n} \right)^{-1/8} \quad (7)$$

where, t_b is the break time relative to T_0 (days), z is the redshift, E_{52} is the isotropic energy E_{iso} in units of 10^{52} erg, $n = 1 \text{ cm}^{-3}$ is the ISM density, and the kinetic energy-to-radiation conversion factor is $\xi = 0.1$ (e.g. Zhang et al. 2007). The jet opening angle will then be: $\theta_j(a) \approx 0.474^{+0.035}_{-0.039}^\circ$, $\theta_j(b) \approx 1.15^{+0.47}_{-0.32}^\circ$ or $\theta_j(c) \approx 2.44^{+0.71}_{-0.35}^\circ$. The typical angle θ_j determined for bursts with a jet break (e.g. Wang et al. 2018) is known to be $\theta_j \approx 2.5 \pm 1.0^\circ$. Thus, the inhomogeneity (flare) in the afterglow light curve is probably not connected with the jet break since the opening angle $\theta_j(a) \sim 0.5^\circ$ would be anomalously narrow. In cases b) and c) the values turn out to be appropriate. At the same time, the opening angle derived from the X-ray data is narrower than from the optical ones. In cases (b) and (c) we will estimate the energy contained within the jet from the formula $E_\gamma = 2\pi(1 - \cos\theta_j)E_{iso}$. We will obtain, $E_{\gamma,O} = 7.04^{+4.72}_{-1.85} \times 10^{51}$ erg when estimated from the optical light curve and $E_{\gamma,X} = 1.55^{+1.51}_{-0.75} \times 10^{51}$ erg when estimated from the X-ray light curve. The gamma factors determined from the X-ray, $\Gamma_X = 197^{+170}_{-99}$, and optical, $\Gamma_O = 120^{+85}_{-34}$ light curves then formally coincide within the error limits.

7.2 Inhomogeneity in the early afterglow

Our previous analysis showed that the light curve of the GRB 200829A afterglow contains a flare-type inhomogeneity at the early phase. The flares in GRB light curves were considered, for example, in the following papers Piro et al. (2005); Perna et al. (2006); Swenson et al. (2013); Yi et al. (2017); Mazaeva et al. (2018). For instance, Swenson et al. (2013) investigated the duration as a function of the flare peak time $\Delta t/t_{peak}$ based on a sample of bursts from the second UVOT/Swift catalog. During the analysis it was established that $\Delta t/t_{peak} < 0.5$ for more than 80% of the bursts from the sample. Yi et al. (2017) and Mazaeva et al. (2018) also established that the flares have a linear $FWHM - t_{peak}$ correlation as well. Figure 14 presents the profile of the flare in the X-ray light curve of GRB 200829A obtained by subtracting the afterglow model.

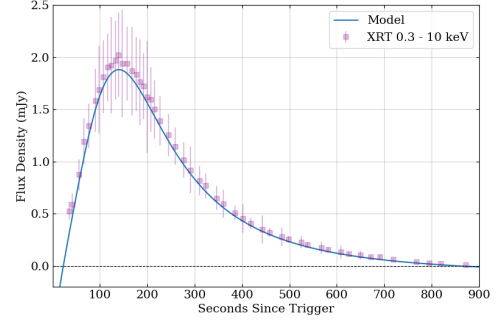


Figure 14. Profile of the flare in the X-ray light curve of GRB 200829A after the afterglow model subtraction. The spectral flux density in mJy is along the vertical axis, while the time since T_0 in seconds is along the horizontal axis. The model is designated by the blue solid line, while the observational data are indicated by the violet squares. The data corresponding to the powerful pulse in the burst prompt phase are not shown.

The flare being investigated in this paper has $FWHM \approx 146$ s and $t_{peak} \approx 132$ s. The values obtained are consistent with the $FWHM - t_{peak}$ correlation (Yi et al. 2017; Mazaeva et al. 2018) and are probably further evidence for the unified physical nature of the flares in GRB light curves. The flares may arise at the shock fed by the burst central engine (Burrows et al. 2005b; de Pasquale et al. 2007; Barkov et al. 2021), from the simultaneous observation of different structured-jet zones (Beniamini et al. 2020; Duque et al. 2022), or a variable accretion rate \dot{M} (e.g. Perna et al. 2006).

Our analysis of the first ~ 250 s of the X-ray light curve for GRB 200829A (Fig. 6) does not reject the hypothesis about a plateau either. Owing to its strong magnetic field, the newly formed magnetar is believed to provide energy pumping and to maintain the luminosity at an approximately constant level for some time equal to the plateau duration (de Pasquale et al. 2007; Metzger et al. 2011; Rowlinson et al. 2013). Let us determine the energy release of the plateau in the X-ray light curve of GRB 200829A. First, we need to determine the plateau fluence in the 0.3–10 keV energy band ($\Delta\nu = 7.3 \times 10^{16} - 2.4 \times 10^{18}$ Hz) from Eq. (8)

$$F_{plat} = \int_{t_1}^{t_2} f_\nu(t) dt \Delta\nu \quad (8)$$

where the times $t_1 = 51.8$ s, and $t_2 = 86.4$ s specify the light curve segment with a power-law slope ~ 0 , corresponding to the plateau, and $f_\nu(t)$ is the spectral flux density. Having substituted all of the necessary values, we obtain the plateau fluence $F_{plat} = 1.3 \times 10^{-10}$ erg cm^{-2} . The plateau energy in the 0.3 – 10 keV band calculated from Eq. (8), will then be $E_{plateau} = 5.8 \times 10^{47}$ erg. Note that such values are consistent with the $L_X - T_a$, where L_x – is the plateau luminosity in the 0.3 - 10 keV, and $T_a = t_2/(1+z)$ is the time at the end of the plateau stage in the source frame (Dainotti et al. 2008, 2021).

Table 4. Parameters of GRB 200829A

R.A. Hours	Dec Degrees	z	E_{iso} 10^{54} erg	$\theta_{j,O}$ °	$\theta_{j,X}$ °	Γ_O	Γ_X	$E_{\gamma,O}$ 10^{51} erg	$E_{\gamma,X}$ 10^{51} erg
16:44:49.14	+72:19:45.63	1.29 ± 0.04	$1.30 \pm +0.01$	$2.44^{+0.18}_{-0.20}$	$1.13^{+0.20}_{-0.27}$	122^{+77}_{-23}	199^{+157}_{-49}	$7.22^{+1.18}_{-1.20}$	$1.59^{+0.60}_{-0.66}$

Table 5. Parameters of the host galaxy

$M_{R,Host}$ mag	$\log SFR$ $M_{\odot} \text{ yr}^{-1}$	M_{Host} $\times 10^9 M_{\odot}$	$A(V)$ mag	N_H $\times 10^{21} \text{ cm}^{-2}$
-19.44	-0.715 ± 0.486	~ 8.5	1.11 ± 0.02	2.6 ± 0.3

8 CONCLUSIONS

The parameters of GRB 200829A and its host galaxy determined in this paper are given in Tables 4 and 5, respectively.

Note some properties of GRB 200829A. In particular, the gamma-ray light curve exhibits a complex structure that is a superposition of pulses with different spectral hardness. Therefore, a proper determination of the spectral lag turned out to be impossible. Our analysis of the gamma-ray BAT/Swift, GBM/Fermi, and SPI-ACS/INTEGRAL data showed that the event belongs to the class of long GRBs (Minaev and Pozanenko 2020a). GRB 200829A is among other ~ 15 most powerful events in isotropic equivalent energy ($E_{iso} \gtrsim 10^{54}$ erg). A plateau gradually transitioning into extended emission with a duration ~ 800 s is traced in the BAT/Swift light curve, while the flux decays as a power law with a slope $\alpha \sim -1$ typical for an afterglow (Mozgunov et al. 2021).

Based on the results of UVOT/Swift and XRT/Swift observations, we made an independent photometric redshift estimate for GRB 200829A, $z = 1.29 \pm 0.04$.

No signature of SN from GRB 200829A was detected during its optical observations within 10 – 40 days after T_0 . The upper limit on the absolute magnitude of SN at maximum $M_R > -23$ is consistent with the well-known absolute magnitude distribution of SNe associated with GRBs (Belkin & Pozanenko 2022).

The host galaxy of GRB 200829A was found with the BTA telescope at SAO RAS. Its absolute magnitude corrected for the Galactic extinction is $M_R \sim -19.44$ at $z = 1.29$, the star formation rate is $\log SFR \sim -0.7 M_{\odot} \text{ yr}^{-1}$, and the mass is $\sim 8 \times 10^9 M_{\odot}$. The absorption on the line of sight is consistent with the linear correlation $N_H \gtrsim 1.6A(V)$ observed in GRB host galaxies (Covino et al. 2013).

A joint analysis of the optical and X-ray observations of the GRB 200829A afterglow showed a chromatic behavior of the early afterglow before the break in the optical light curve (about 0.15 days since the GBM/Fermi trigger). The presence of a chromatic feature is consistent with the model of a structured jet.

ACKNOWLEDGMENTS

N.S. Pankov, A.S. Pozanenko, P.Yu. Minaev, S.O. Belkin, E.V. Klunko, and A.A. Volnova thank the Ministry of Ed-

ucation and Science of the Russian Federation for its financial support, project no. 075-15-2022-1221 (2022-BRICS-8847-2335). This work made use of data supplied by the UK Swift Science Data Centre at the University of Leicester. Based on observations made with the Nordic Optical Telescope, owned in collaboration by the University of Turku and Aarhus University, and operated jointly by Aarhus University, the University of Turku and the University of Oslo, representing Denmark, Finland and Norway, the University of Iceland and Stockholm University at the Observatorio del Roque de los Muchachos, La Palma, Spain, of the Instituto de Astrofísica de Canarias.

REFERENCES

- Amati L., et al., 2002, *A&A*, **390**, 81
Band D., et al., 1993, *ApJ*, **413**, 281
Barkov M. V., Luo Y., Lyutikov M., 2021, *ApJ*, **907**, 109
Belkin S., Pozanenko A., 2022, in Pozanenko A., Stupnikov S., Thalheim B., Mendez E., Kiselyova N., eds, Data Analytics and Management in Data Intensive Domains. Springer International Publishing, Cham, pp 74–91
Belkin S. O., et al., 2020, *Astronomy Letters*, **46**, 783
Beniamini P., Duque R., Daigne F., Mochkovitch R., 2020, *MNRAS*, **492**, 2847
Bennett C. L., Larson D., Weiland J. L., Hinshaw G., 2014, *ApJ*, **794**, 135
Beuermann K., et al., 1999, *A&A*, **352**, L26
Bisnovatyi-Kogan G. S., Imshennik V. S., Nadyozhin D. K., Chechetkin V. M., 1975, *Ap&SS*, **35**, 3
Blackburn J. K., 1995, in Shaw R. A., Payne H. E., Hayes J. J. E., eds, *Astronomical Society of the Pacific Conference Series Vol. 77, Astronomical Data Analysis Software and Systems IV*. p. 367
Burrows D. N., et al., 2005a, *Space Sci. Rev.*, **120**, 165
Burrows D. N., et al., 2005b, *Science*, **309**, 1833
Butler N. R., Kocevski D., Bloom J. S., Curtis J. L., 2007, *ApJ*, **671**, 656
Chambers K. C., et al., 2016, arXiv e-prints, p. [arXiv:1612.05560](https://arxiv.org/abs/1612.05560)
Colgate S. A., 1968, *Canadian Journal of Physics Supplement*, **46**, 476
Covino S., et al., 2013, *MNRAS*, **432**, 1231
Daigne F., Rossi E. M., Mochkovitch R., 2006, *MNRAS*, **372**, 1034
Dainotti M. G., Cardone V. F., Capozziello S., 2008, *MNRAS*, **391**, L79
Dainotti M. G., Lenart A. Ł., Fraija N., Nagataki S., Warren D. C., De Simone B., Srinivasaragavan G., Mata A., 2021, *PASJ*, **73**, 970

- Dainotti M. G., et al., 2022, *ApJS*, **261**, 25
- De Pasquale M., et al., 2016, *MNRAS*, **455**, 1027
- Derebi-Bégué H., Pe'er A., Ryde F., Oates S. R., Zhang B., Dainotti M. G., 2022, *Nature Communications*, **13**, 5611
- Devyatkin A. V., Gorshanov D. L., Kouprianov V. V., Verestchagina I. A., 2010, *Solar System Research*, **44**, 68
- Duque R., Beniamini P., Daigne F., Mochkovitch R., 2022, *MNRAS*, **513**, 951
- Eichler D., Levinson A., 2004, *ApJ*, **614**, L13
- Evans P. A., et al., 2007, *A&A*, **469**, 379
- Evans P. A., et al., 2009, *MNRAS*, **397**, 1177
- Goad M. R., Osborne J. P., Beardmore A. P., Evans P. A., Swift-XRT Team 2020, GRB Coordinates Network, **28313**, 1
- Gruber D., et al., 2014, *ApJS*, **211**, 12
- HI4PI Collaboration et al., 2016, *A&A*, **594**, A116
- Hakkila J., Preece R. D., 2011, *ApJ*, **740**, 104
- Han S., Li X., Jiang L., Jin Z., He H., Wang Y., Wei D., 2022, *Universe*, **8**
- Hill J. E., et al., 2006, *ApJ*, **639**, 303
- Izzo L., 2020, GRB Coordinates Network, **28331**, 1
- Kaneko Y., Preece R. D., Briggs M. S., Paciesas W. S., Meegan C. A., Band D. L., 2006, *ApJS*, **166**, 298
- Komissarov S. S., Vlahakis N., Königl A., Barkov M. V., 2009, *MNRAS*, **394**, 1182
- Koshut T. M., Paciesas W. S., Kouveliotou C., van Paradijs J., Pendleton G. N., Fishman G. J., Meegan C. A., 1996, *ApJ*, **463**, 570
- Kouprianov V., 2012, in 39th COSPAR Scientific Assembly. p. 974
- Kouveliotou C., Meegan C. A., Fishman G. J., Bhat N. P., Briggs M. S., Koshut T. M., Paciesas W. S., Pendleton G. N., 1993, *ApJ*, **413**, L101
- Kuin N. P. M., Siegel M. H., Swift/UVOT Team 2020, GRB Coordinates Network, **28311**, 1
- Kumar P., Zhang B., 2015, *Physics Reports*, **561**, 1
- Lamb G. P., Kann D. A., Fernández J. J., Mandel I., Levan A. J., Tanvir N. R., 2021, *MNRAS*, **506**, 4163
- Lazzati D., et al., 2001, *A&A*, **378**, 996
- Levan A., 2018, Gamma-Ray Bursts. AAS-IOP astronomy, Institute of Physics Publishing, <https://books.google.ru/books?id=sx-RtAEACAAJ>
- Levinson A., Eichler D., 2005, *ApJ*, **629**, L13
- Lien A., et al., 2016, *ApJ*, **829**, 7
- Luchkov B. I., Mitrofanov I. G., Rozental' I. L., 1996, *Physics-Uspekhi*, **39**, 695
- Mahajan S., et al., 2018, *MNRAS*, **475**, 788
- Masetti N., et al., 2005, *A&A*, **438**, 841
- Mazaeva E., Pozanenko A., Minaev P., 2018, *International Journal of Modern Physics D*, **27**, 1844012
- Mazzali P. A., et al., 2003, *ApJ*, **599**, L95
- Metzger B. D., Giannios D., Thompson T. A., Bucciantini N., Quataert E., 2011, *MNRAS*, **413**, 2031
- Minaev P. Y., Pozanenko A. S., 2017, *Astronomy Letters*, **43**, 1
- Minaev P. Y., Pozanenko A. S., 2020a, *Astronomy Letters*, **46**, 573
- Minaev P. Y., Pozanenko A. S., 2020b, *MNRAS*, **492**, 1919
- Minaev P. Y., Pozanenko A. S., 2021, *MNRAS*, **504**, 926
- Minaev P. Y., Pozanenko A. S., Loznikov V. M., 2010a, *Astronomy Letters*, **36**, 707
- Minaev P. Y., Pozanenko A. S., Loznikov V. M., 2010b, *Astrophysical Bulletin*, **65**, 326
- Minaev P. Y., Pozanenko A. S., Molkov S. V., Grebenev S. A., 2014, *Astronomy Letters*, **40**, 235
- Monet D. G., et al., 2003, *AJ*, **125**, 984
- Moskvitin A. S., Aitov V. N., GRB follow-up Team 2020a, GRB Coordinates Network, **28322**, 1
- Moskvitin A. S., Aitov V. N., GRB follow-up Team 2020b, GRB Coordinates Network, **28328**, 1
- Mozgunov G. Y., Minaev P. Y., Pozanenko A. S., 2021, *Astronomy Letters*, **47**, 150
- Newville M., et al., 2021, *lmfit/lmfit-py*: 1.0.3, [doi:10.5281/zenodo.5570790](https://doi.org/10.5281/zenodo.5570790), <https://doi.org/10.5281/zenodo.5570790>
- Norris J. P., Bonnell J. T., Kazanas D., Scargle J. D., Hakkila J., Giblin T. W., 2005, *ApJ*, **627**, 324
- Oates S. R., et al., 2011, *MNRAS*, **412**, 561
- Oates S. R., Kuin N. P. M., De Pasquale M., Campana S., Tohuvavohu A., Siegel M. H., Neil Gehrels Swift Observatory Team 2020, GRB Coordinates Network, **28338**, 1
- Paczynski B., 1986, *ApJ*, **308**, L43
- Paczyński B., 1998, in Meegan C. A., Preece R. D., Koshut T. M., eds, American Institute of Physics Conference Series Vol. 428, Gamma-Ray Bursts, 4th Hunstville Symposium. pp 783–787 ([arXiv:astro-ph/9706232](https://arxiv.org/abs/astro-ph/9706232)), [doi:10.1063/1.55404](https://doi.org/10.1063/1.55404)
- Pankov N., et al., 2020, GRB Coordinates Network, **28329**, 1
- Pankov N., Pozanenko A., Kouprianov V., Belkin S., 2022, in Pozanenko A., Stupnikov S., Thalheim B., Mendez E., Kiselyova N., eds, Data Analytics and Management in Data Intensive Domains. Springer International Publishing, Cham, pp 104–134
- Pei Y. C., 1992, *ApJ*, **395**, 130
- Perna R., Armitage P. J., Zhang B., 2006, *ApJ*, **636**, L29
- Piran T., 2004, *Reviews of Modern Physics*, **76**, 1143
- Piro L., et al., 2005, *ApJ*, **623**, 314
- Postnov K. A., 1999, *Phys. Usp.*, **42**, 469
- Pozanenko A. S., Rumyantsev V. V., Loznikov V. M., Volnova A. A., Shulga A. P., 2008, *Astronomy Letters*, **34**, 141
- Pozanenko A. S., et al., 2018, *ApJ*, **852**, L30
- Pozanenko A., Reva I., Serebryanskiy A., Belkin S., Krugov M., Mazaeva E., Volnova A., IKI-GRB-FuN 2020, GRB Coordinates Network, **28308**, 1
- Pozanenko A. S., Barkov M. V., Minaev P. Y., Volnova A. A., 2021, *Astronomy Letters*, **47**, 791
- Prilutskii O. F., Usov V. V., 1975, *Ap&SS*, **34**, 395
- Resmi L., et al., 2012, *MNRAS*, **427**, 288
- Rowlinson A., O'Brien P. T., Metzger B. D., Tanvir N. R., Levan A. J., 2013, *MNRAS*, **430**, 1061
- Rozental I. L., Usov V. V., Estulin I. V., 1983, *Uspekhi Fizicheskikh Nauk*, **140**, 97
- Sari R., Piran T., Halpern J. P., 1999, *ApJ*, **519**, L17
- Schady P., et al., 2010, *MNRAS*, **401**, 2773
- Schlaflly E. F., Finkbeiner D. P., 2011, *ApJ*, **737**, 103
- Schlegel D. J., Finkbeiner D. P., Davis M., 1998, *ApJ*, **500**, 525
- Science Software Branch at STScI 2012, PyRAF: Python alternative for IRAF, Astrophysics Source Code Library, record ascl:1207.011 (ascl:1207.011)
- Siegel M. H., Gropp J. D., Kennea J. A., Kuin N. P. M., Laha S., Sbarufatti B., Neil Gehrels Swift Observatory Team 2020, GRB Coordinates Network, **28307**, 1
- Swenson C. A., Roming P. W. A., De Pasquale M., Oates S. R., 2013, *ApJ*, **774**, 2
- Tsvetkova A., et al., 2017, *ApJ*, **850**, 161
- Tsvetkova A., et al., 2021, *ApJ*, **908**, 83
- Vinko J., Vida K., Pal A., Kriskovics L., Szakats R., Ordasi A., Sarneczky K., 2020, GRB Coordinates Network, **28316**, 1
- Volnova A. A., et al., 2014, *MNRAS*, **442**, 2586
- Volnova A. A., et al., 2017, *MNRAS*, **467**, 3500
- Volnova A., Pozanenko A., Mazaeva E., Belkin S., Minaev P., 2021, in Sychev A., Makhortov S., Thalheim B., eds, Data Analytics and Management in Data Intensive Domains. Springer International Publishing, Cham, pp 148–159
- Wang L., Wheeler J. C., 1998, *ApJ*, **504**, L87
- Wang X.-G., Zhang B., Liang E.-W., Lu R.-J., Lin D.-B., Li J., Li L., 2018, *ApJ*, **859**, 160
- Woosley S. E., 1993, *ApJ*, **405**, 273
- Woosley S. E., Eastman R. G., Schmidt B. P., 1999, *ApJ*, **516**, 788
- Yi S.-X., Yu H., Wang F. Y., Dai Z.-G., 2017, *ApJ*, **844**, 79
- Yu Y.-W., Gao H., Wang F.-Y., Zhang B.-B., 2022, arXiv e-prints, p. [arXiv:2204.04417](https://arxiv.org/abs/2204.04417)

- Zhang B., Zhang B.-B., Liang E.-W., Gehrels N., Burrows D. N., Mészáros P., 2007, [ApJ](#), **655**, L25
- Zhu Z. P., Y Fu S., Liu X., Xu D., Gao X., Zhang X., Liu J. Z., 2020a, GRB Coordinates Network, [28324](#), 1
- Zhu Z. P., Y Fu S., Liu X., Xu D., Gao X., Zhang X., Liu J. Z., 2020b, GRB Coordinates Network, [28330](#), 1
- de Pasquale M., et al., 2007, [MNRAS](#), **377**, 1638
- von Kienlin A., Beckmann V., Rau A., et al. 2003, [A&A](#), **411**, L299
- von Kienlin A., et al., 2020, [ApJ](#), **893**, 46

Table 1. Log of optical observations. The magnitudes in the UVOT/Swift *u*, *b*, *v*, *uvw1*, *uvw2*, *white*, *Clear*, *R*, and *I* filters are given in the Vega photometric system, those in the *g*, *r*, *i*, and *z* filters are given in the AB photometric system. The values are given without any correction for the extinction in the Galaxy and the GRB 200829A host galaxy. Continue in Table 2.

$t - T_0$ days	Magnitude	Flux density mJy	Observatory/Telescope	Filter	GCN no.
0.002361	13.88 ± 0.08	10.213 ^{+0.777} _{-0.777}	Swift/UVOT	v	-
0.003391	14.33 ± 0.07	3.566 ^{+0.689} _{-0.689}	Swift/UVOT	white	-
0.003391	14.33 ± 0.07	3.566 ^{+0.689} _{-0.689}	Swift/UVOT	white	-
0.005810	14.55 ± 0.05	2.189 ^{+0.104} _{-0.104}	Swift/UVOT	u	-
0.007431	15.82 ± 0.08	1.906 ^{+0.134} _{-0.134}	Swift/UVOT	b	-
0.007720	15.46 ± 0.08	1.263 ^{+0.248} _{-0.248}	Swift/UVOT	white	-
0.008009	17.04 ± 0.28	0.113 ^{+0.029} _{-0.029}	Swift/UVOT	uvw2	-
0.008299	15.43 ± 0.10	2.454 ^{+0.230} _{-0.230}	Swift/UVOT	v	-
0.008866	15.46 ± 0.14	0.582 ^{+0.074} _{-0.074}	Swift/UVOT	uvw1	-
0.009155	15.08 ± 0.09	1.339 ^{+0.103} _{-0.103}	Swift/UVOT	u	-
0.009444	16.13 ± 0.09	1.430 ^{+0.112} _{-0.112}	Swift/UVOT	b	-
0.009734	15.66 ± 0.08	1.049 ^{+0.206} _{-0.206}	Swift/UVOT	white	-
0.010023	18.37 ± 0.52	0.033 ^{+0.016} _{-0.016}	Swift/UVOT	uvw2	-
0.010301	15.89 ± 0.12	1.599 ^{+0.182} _{-0.182}	Swift/UVOT	v	-
0.010880	15.63 ± 0.14	0.497 ^{+0.067} _{-0.067}	Swift/UVOT	uvw1	-
0.011944	16.00 ± 0.07	0.768 ^{+0.148} _{-0.148}	Swift/UVOT	white	-
0.013275	16.20 ± 0.14	1.205 ^{+0.157} _{-0.157}	Swift/UVOT	v	-
0.013843	16.08 ± 0.17	0.330 ^{+0.053} _{-0.053}	Swift/UVOT	uvw1	-
0.014120	15.55 ± 0.10	0.869 ^{+0.077} _{-0.077}	Swift/UVOT	u	-
0.014410	16.39 ± 0.10	1.131 ^{+0.097} _{-0.097}	Swift/UVOT	b	-
0.014688	16.29 ± 0.09	0.590 ^{+0.117} _{-0.117}	Swift/UVOT	white	-
0.015324	16.32 ± 0.20	1.081 ^{+0.198} _{-0.198}	Swift/UVOT	v	-
0.015845	16.13 ± 0.18	0.316 ^{+0.051} _{-0.051}	Swift/UVOT	uvw1	-
0.016123	15.80 ± 0.11	0.693 ^{+0.066} _{-0.066}	Swift/UVOT	u	-
0.016458	16.47 ± 0.12	1.049 ^{+0.117} _{-0.117}	Swift/UVOT	b	-
0.016701	16.26 ± 0.09	0.602 ^{+0.119} _{-0.119}	Swift/UVOT	white	-
0.016991	18.24 ± 0.48	0.037 ^{+0.017} _{-0.017}	Swift/UVOT	uvw2	-
0.017280	16.41 ± 0.16	0.991 ^{+0.141} _{-0.141}	Swift/UVOT	v	-
0.017847	16.84 ± 0.24	0.163 ^{+0.036} _{-0.036}	Swift/UVOT	uvw1	-
0.018148	16.03 ± 0.11	0.559 ^{+0.058} _{-0.058}	Swift/UVOT	u	-
0.018438	16.82 ± 0.11	0.759 ^{+0.077} _{-0.077}	Swift/UVOT	b	-
0.018727	16.42 ± 0.09	0.519 ^{+0.103} _{-0.103}	Swift/UVOT	white	-
0.019306	16.63 ± 0.17	0.809 ^{+0.128} _{-0.128}	Swift/UVOT	v	-
0.019873	16.36 ± 0.19	0.255 ^{+0.046} _{-0.046}	Swift/UVOT	uvw1	-
0.020150	15.99 ± 0.11	0.582 ^{+0.060} _{-0.060}	Swift/UVOT	u	-
0.020440	16.81 ± 0.11	0.768 ^{+0.077} _{-0.077}	Swift/UVOT	b	-
0.035551	16.29 ± 0.13	0.864 ^{+0.100} _{-0.113}	TShAO/Zeiss-1000	R	-
0.036296	16.34 ± 0.08	0.828 ^{+0.061} _{-0.066}	TShAO/Zeiss-1000	R	-
0.037041	16.25 ± 0.12	0.898 ^{+0.092} _{-0.103}	TShAO/Zeiss-1000	R	-
0.037785	16.37 ± 0.11	0.805 ^{+0.076} _{-0.084}	TShAO/Zeiss-1000	R	-
0.038524	16.41 ± 0.10	0.773 ^{+0.066} _{-0.072}	TShAO/Zeiss-1000	R	-
0.039271	16.36 ± 0.08	0.810 ^{+0.059} _{-0.064}	TShAO/Zeiss-1000	R	-
0.040015	16.37 ± 0.07	0.802 ^{+0.053} _{-0.057}	TShAO/Zeiss-1000	R	-
0.040756	16.43 ± 0.07	0.763 ^{+0.046} _{-0.049}	TShAO/Zeiss-1000	R	-
0.041500	16.42 ± 0.05	0.771 ^{+0.037} _{-0.039}	TShAO/Zeiss-1000	R	-
0.042240	16.45 ± 0.05	0.747 ^{+0.034} _{-0.035}	TShAO/Zeiss-1000	R	-
0.042984	16.45 ± 0.06	0.750 ^{+0.041} _{-0.043}	TShAO/Zeiss-1000	R	-
0.043734	16.49 ± 0.08	0.718 ^{+0.053} _{-0.057}	TShAO/Zeiss-1000	R	-
0.044479	16.48 ± 0.07	0.724 ^{+0.046} _{-0.050}	TShAO/Zeiss-1000	R	-
0.045224	16.42 ± 0.07	0.765 ^{+0.050} _{-0.054}	TShAO/Zeiss-1000	R	-
0.045982	16.51 ± 0.06	0.704 ^{+0.035} _{-0.037}	TShAO/Zeiss-1000	R	-
0.046728	16.52 ± 0.07	0.699 ^{+0.045} _{-0.049}	TShAO/Zeiss-1000	R	-
0.047472	16.55 ± 0.06	0.682 ^{+0.038} _{-0.041}	TShAO/Zeiss-1000	R	-
0.048218	16.54 ± 0.08	0.691 ^{+0.050} _{-0.054}	TShAO/Zeiss-1000	R	-
0.048963	16.58 ± 0.06	0.662 ^{+0.038} _{-0.040}	TShAO/Zeiss-1000	R	-
0.049708	16.54 ± 0.07	0.689 ^{+0.041} _{-0.044}	TShAO/Zeiss-1000	R	-
0.050451	16.52 ± 0.05	0.697 ^{+0.032} _{-0.034}	TShAO/Zeiss-1000	R	-

Table 2. Log of optical observations. Continue in Table 3.

$t - T_0$ days	Magnitude	Flux density mJy	Observatory/Telescope	Filter	GCN no.
0.051197	16.51 ± 0.07	$0.706^{+0.043}_{-0.046}$	TShAO/Zeiss-1000	R	-
0.051941	16.55 ± 0.08	$0.679^{+0.048}_{-0.052}$	TShAO/Zeiss-1000	R	-
0.052685	16.64 ± 0.08	$0.628^{+0.046}_{-0.050}$	TShAO/Zeiss-1000	R	-
0.053429	16.66 ± 0.07	$0.618^{+0.037}_{-0.040}$	TShAO/Zeiss-1000	R	-
0.054173	16.64 ± 0.08	$0.630^{+0.043}_{-0.046}$	TShAO/Zeiss-1000	R	-
0.054916	16.66 ± 0.08	$0.618^{+0.043}_{-0.047}$	TShAO/Zeiss-1000	R	-
0.055662	16.64 ± 0.08	$0.624^{+0.046}_{-0.050}$	TShAO/Zeiss-1000	R	-
0.056408	16.69 ± 0.07	$0.599^{+0.035}_{-0.037}$	TShAO/Zeiss-1000	R	-
0.057151	16.68 ± 0.06	$0.602^{+0.034}_{-0.036}$	TShAO/Zeiss-1000	R	-
0.057897	16.67 ± 0.07	$0.610^{+0.040}_{-0.042}$	TShAO/Zeiss-1000	R	-
0.058641	16.72 ± 0.06	$0.583^{+0.029}_{-0.030}$	TShAO/Zeiss-1000	R	-
0.059387	16.66 ± 0.08	$0.616^{+0.044}_{-0.048}$	TShAO/Zeiss-1000	R	-
0.060131	16.71 ± 0.07	$0.588^{+0.034}_{-0.036}$	TShAO/Zeiss-1000	R	-
0.060873	16.74 ± 0.08	$0.571^{+0.039}_{-0.042}$	TShAO/Zeiss-1000	R	-
0.061146	17.50 ± 0.08	$0.192^{+0.038}_{-0.038}$	Swift/UVOT	white	-
0.061617	16.75 ± 0.08	$0.566^{+0.039}_{-0.042}$	TShAO/Zeiss-1000	R	-
0.062361	16.73 ± 0.07	$0.575^{+0.035}_{-0.038}$	TShAO/Zeiss-1000	R	-
0.063109	16.75 ± 0.08	$0.569^{+0.040}_{-0.043}$	TShAO/Zeiss-1000	R	-
0.065139	16.76 ± 0.09	$0.560^{+0.046}_{-0.051}$	TShAO/Zeiss-1000	R	-
0.065887	16.77 ± 0.07	$0.555^{+0.035}_{-0.037}$	TShAO/Zeiss-1000	R	-
0.066630	16.77 ± 0.07	$0.554^{+0.036}_{-0.038}$	TShAO/Zeiss-1000	R	-
0.067374	16.82 ± 0.06	$0.531^{+0.027}_{-0.028}$	TShAO/Zeiss-1000	R	-
0.068041	16.88 ± 0.19	$0.502^{+0.079}_{-0.093}$	Kitab-ISON/RC36	Clear	-
0.068117	16.92 ± 0.08	$0.483^{+0.033}_{-0.035}$	TShAO/Zeiss-1000	R	-
0.068863	16.78 ± 0.07	$0.551^{+0.034}_{-0.036}$	TShAO/Zeiss-1000	R	-
0.069605	16.77 ± 0.09	$0.555^{+0.043}_{-0.046}$	TShAO/Zeiss-1000	R	-
0.070350	16.86 ± 0.07	$0.515^{+0.030}_{-0.032}$	TShAO/Zeiss-1000	R	-
0.071093	16.86 ± 0.08	$0.512^{+0.035}_{-0.037}$	TShAO/Zeiss-1000	R	-
0.071839	16.81 ± 0.05	$0.536^{+0.024}_{-0.025}$	TShAO/Zeiss-1000	R	-
0.072582	16.89 ± 0.09	$0.499^{+0.041}_{-0.045}$	TShAO/Zeiss-1000	R	-
0.073053	16.79 ± 0.21	$0.548^{+0.098}_{-0.120}$	Kitab-ISON/RC36	Clear	-
0.073328	16.89 ± 0.09	$0.498^{+0.039}_{-0.043}$	TShAO/Zeiss-1000	R	-
0.074074	16.92 ± 0.08	$0.485^{+0.036}_{-0.039}$	TShAO/Zeiss-1000	R	-
0.074818	16.87 ± 0.08	$0.508^{+0.036}_{-0.039}$	TShAO/Zeiss-1000	R	-
0.075561	16.88 ± 0.09	$0.503^{+0.038}_{-0.041}$	TShAO/Zeiss-1000	R	-
0.076305	16.95 ± 0.09	$0.473^{+0.038}_{-0.041}$	TShAO/Zeiss-1000	R	-
0.077049	16.90 ± 0.09	$0.493^{+0.041}_{-0.044}$	TShAO/Zeiss-1000	R	-
0.077791	16.96 ± 0.09	$0.465^{+0.039}_{-0.042}$	TShAO/Zeiss-1000	R	-
0.078076	17.11 ± 0.18	$0.407^{+0.061}_{-0.072}$	Kitab-ISON/RC36	Clear	-
0.078532	16.97 ± 0.07	$0.463^{+0.031}_{-0.033}$	TShAO/Zeiss-1000	R	-
0.079277	16.94 ± 0.07	$0.478^{+0.030}_{-0.032}$	TShAO/Zeiss-1000	R	-
0.080020	16.93 ± 0.07	$0.481^{+0.032}_{-0.034}$	TShAO/Zeiss-1000	R	-
0.080766	17.03 ± 0.09	$0.438^{+0.033}_{-0.036}$	TShAO/Zeiss-1000	R	-
0.081412	17.65 ± 0.08	$0.168^{+0.033}_{-0.033}$	Swift/UVOT	white	-
0.081512	16.95 ± 0.07	$0.470^{+0.031}_{-0.034}$	TShAO/Zeiss-1000	R	-
0.082256	17.05 ± 0.08	$0.428^{+0.032}_{-0.034}$	TShAO/Zeiss-1000	R	-
0.083000	17.01 ± 0.08	$0.446^{+0.033}_{-0.035}$	TShAO/Zeiss-1000	R	-
0.083099	17.27 ± 0.28	$0.350^{+0.079}_{-0.103}$	Kitab-ISON/RC36	Clear	-
0.083745	17.02 ± 0.09	$0.441^{+0.035}_{-0.038}$	TShAO/Zeiss-1000	R	-
0.084490	17.00 ± 0.10	$0.452^{+0.040}_{-0.044}$	TShAO/Zeiss-1000	R	-
0.085234	17.06 ± 0.09	$0.425^{+0.033}_{-0.036}$	TShAO/Zeiss-1000	R	-
0.085977	17.03 ± 0.09	$0.438^{+0.034}_{-0.037}$	TShAO/Zeiss-1000	R	-
0.086720	16.99 ± 0.09	$0.456^{+0.038}_{-0.041}$	TShAO/Zeiss-1000	R	-
0.087465	17.00 ± 0.06	$0.449^{+0.024}_{-0.026}$	TShAO/Zeiss-1000	R	-
0.088110	17.31 ± 0.29	$0.340^{+0.079}_{-0.102}$	Kitab-ISON/RC36	Clear	-
0.088206	17.04 ± 0.07	$0.433^{+0.025}_{-0.027}$	TShAO/Zeiss-1000	R	-
0.088952	16.97 ± 0.06	$0.463^{+0.025}_{-0.026}$	TShAO/Zeiss-1000	R	-
0.089692	17.08 ± 0.09	$0.418^{+0.034}_{-0.037}$	TShAO/Zeiss-1000	R	-
0.090437	17.09 ± 0.08	$0.413^{+0.028}_{-0.030}$	TShAO/Zeiss-1000	R	-

Table 3. Log of optical observations. Continue in Table 4.

$t - T_0$ days	Magnitude	Flux density mJy	Observatory/Telescope	Filter	GCN no.
0.091182	17.05 ± 0.09	$0.431^{+0.033}_{-0.036}$	TShAO/Zeiss-1000	R	-
0.091927	17.09 ± 0.07	$0.413^{+0.027}_{-0.029}$	TShAO/Zeiss-1000	R	-
0.092672	17.04 ± 0.09	$0.435^{+0.036}_{-0.039}$	TShAO/Zeiss-1000	R	-
0.093134	16.81 ± 0.17	$0.535^{+0.076}_{-0.088}$	Kitab-ISON/RC36	Clear	-
0.093926	17.14 ± 0.08	$0.397^{+0.029}_{-0.031}$	TShAO/Zeiss-1000	R	-
0.094673	17.19 ± 0.10	$0.379^{+0.032}_{-0.036}$	TShAO/Zeiss-1000	R	-
0.095420	17.19 ± 0.08	$0.377^{+0.028}_{-0.030}$	TShAO/Zeiss-1000	R	-
0.096163	17.00 ± 0.06	$0.452^{+0.025}_{-0.027}$	TShAO/Zeiss-1000	R	-
0.098157	16.86 ± 0.17	$0.510^{+0.074}_{-0.087}$	Kitab-ISON/RC36	Clear	-
0.103180	16.82 ± 0.22	$0.532^{+0.098}_{-0.121}$	Kitab-ISON/RC36	Clear	-
0.108203	17.15 ± 0.22	$0.391^{+0.072}_{-0.088}$	Kitab-ISON/RC36	Clear	-
0.113215	17.11 ± 0.23	$0.407^{+0.079}_{-0.097}$	Kitab-ISON/RC36	Clear	-
0.118238	17.39 ± 0.27	$0.314^{+0.068}_{-0.087}$	Kitab-ISON/RC36	Clear	-
0.119339	17.29 ± 0.08	$0.344^{+0.024}_{-0.026}$	TShAO/Zeiss-1000	R	-
0.120315	17.33 ± 0.07	$0.333^{+0.022}_{-0.023}$	TShAO/Zeiss-1000	R	-
0.121292	17.26 ± 0.08	$0.356^{+0.025}_{-0.026}$	TShAO/Zeiss-1000	R	-
0.122265	17.39 ± 0.06	$0.314^{+0.018}_{-0.019}$	TShAO/Zeiss-1000	R	-
0.123244	17.33 ± 0.07	$0.334^{+0.020}_{-0.022}$	TShAO/Zeiss-1000	R	-
0.123261	17.17 ± 0.24	$0.385^{+0.077}_{-0.097}$	Kitab-ISON/RC36	Clear	-
0.124219	17.43 ± 0.08	$0.302^{+0.021}_{-0.022}$	TShAO/Zeiss-1000	R	-
0.125192	17.30 ± 0.08	$0.341^{+0.026}_{-0.028}$	TShAO/Zeiss-1000	R	-
0.126167	17.44 ± 0.10	$0.301^{+0.026}_{-0.029}$	TShAO/Zeiss-1000	R	-
0.127143	17.39 ± 0.08	$0.314^{+0.021}_{-0.023}$	TShAO/Zeiss-1000	R	-
0.128123	17.45 ± 0.08	$0.299^{+0.022}_{-0.024}$	TShAO/Zeiss-1000	R	-
0.128284	17.16 ± 0.22	$0.389^{+0.071}_{-0.087}$	Kitab-ISON/RC36	Clear	-
0.129104	17.37 ± 0.07	$0.321^{+0.019}_{-0.021}$	TShAO/Zeiss-1000	R	-
0.130078	17.38 ± 0.09	$0.318^{+0.025}_{-0.027}$	TShAO/Zeiss-1000	R	-
0.131051	17.46 ± 0.10	$0.294^{+0.026}_{-0.028}$	TShAO/Zeiss-1000	R	-
0.132032	17.45 ± 0.10	$0.298^{+0.026}_{-0.029}$	TShAO/Zeiss-1000	R	-
0.133003	17.49 ± 0.09	$0.287^{+0.023}_{-0.025}$	TShAO/Zeiss-1000	R	-
0.133978	17.34 ± 0.08	$0.328^{+0.025}_{-0.027}$	TShAO/Zeiss-1000	R	-
0.134954	17.36 ± 0.10	$0.322^{+0.027}_{-0.030}$	TShAO/Zeiss-1000	R	-
0.135935	17.40 ± 0.07	$0.312^{+0.019}_{-0.020}$	TShAO/Zeiss-1000	R	-
0.136912	17.23 ± 0.09	$0.364^{+0.029}_{-0.031}$	TShAO/Zeiss-1000	R	-
0.137886	17.36 ± 0.09	$0.323^{+0.025}_{-0.028}$	TShAO/Zeiss-1000	R	-
0.138562	17.31 ± 0.26	$0.340^{+0.073}_{-0.093}$	Kitab-ISON/RC36	Clear	-
0.141863	17.58 ± 0.09	$0.224^{+0.018}_{-0.019}$	Koshka (INASAN)/Zeiss-1000	I	-
0.143123	17.72 ± 0.09	$0.250^{+0.035}_{-0.036}$	Koshka (INASAN)/Zeiss-1000	R	-
0.147173	17.30 ± 0.19	$0.342^{+0.054}_{-0.064}$	Kitab-ISON/RC36	Clear	-
0.148628	17.45 ± 0.10	$0.296^{+0.027}_{-0.029}$	TShAO/Zeiss-1000	R	-
0.149606	17.44 ± 0.14	$0.301^{+0.036}_{-0.040}$	TShAO/Zeiss-1000	R	-
0.150584	17.57 ± 0.12	$0.266^{+0.028}_{-0.031}$	TShAO/Zeiss-1000	R	-
0.151559	17.36 ± 0.11	$0.324^{+0.030}_{-0.033}$	TShAO/Zeiss-1000	R	-
0.152531	17.53 ± 0.10	$0.276^{+0.024}_{-0.026}$	TShAO/Zeiss-1000	R	-
0.153510	17.52 ± 0.11	$0.279^{+0.027}_{-0.029}$	TShAO/Zeiss-1000	R	-
0.154643	17.72 ± 0.10	$0.249^{+0.036}_{-0.037}$	Koshka (INASAN)/Zeiss-1000	R	-
0.154643	17.71 ± 0.13	$0.199^{+0.022}_{-0.025}$	Koshka (INASAN)/Zeiss-1000	I	-
0.158932	17.48 ± 0.22	$0.289^{+0.053}_{-0.066}$	Kitab-ISON/RC36	Clear	-
0.169696	17.11 ± 0.17	$0.408^{+0.060}_{-0.071}$	Kitab-ISON/RC36	Clear	-
0.176090	17.65 ± 0.09	$0.210^{+0.017}_{-0.018}$	SAO RAS/Zeiss-1000	I	28322
0.177833	18.03 ± 0.11	$0.211^{+0.047}_{-0.048}$	CrAO/AZT-11	R	-
0.180448	17.57 ± 0.24	$0.266^{+0.053}_{-0.066}$	Kitab-ISON/RC36	Clear	-
0.182092	17.71 ± 0.10	$0.233^{+0.021}_{-0.023}$	CrAO/AZT-11	R	-
0.182093	17.91 ± 0.09	$0.231^{+0.047}_{-0.048}$	CrAO/AZT-11	R	-
0.185933	17.90 ± 0.09	$0.167^{+0.013}_{-0.014}$	Koshka (INASAN)/Zeiss-1000	I	-
0.186352	17.81 ± 0.10	$0.213^{+0.018}_{-0.020}$	CrAO/AZT-11	R	-
0.186353	18.01 ± 0.12	$0.214^{+0.048}_{-0.049}$	CrAO/AZT-11	R	-
0.190413	18.00 ± 0.08	$0.197^{+0.032}_{-0.033}$	Koshka (INASAN)/Zeiss-1000	R	-
0.190611	17.73 ± 0.10	$0.229^{+0.020}_{-0.022}$	CrAO/AZT-11	R	-

Table 4. Log of optical observations, last table.

$t - T_0$ days	Magnitude	Flux density mJy	Observatory/Telescope	Filter	GCN no.
0.190613	17.99 ± 0.11	$0.218^{+0.048}_{-0.049}$	CrAO/AZT-11	R	-
0.194870	17.80 ± 0.10	$0.215^{+0.019}_{-0.021}$	CrAO/AZT-11	R	-
0.194873	18.11 ± 0.13	$0.199^{+0.048}_{-0.049}$	CrAO/AZT-11	R	-
0.196467	17.68 ± 0.21	$0.241^{+0.042}_{-0.051}$	Kitab-ISON/RC36	Clear	-
0.215673	18.04 ± 0.10	$0.147^{+0.013}_{-0.014}$	Koshka (INASAN)/Zeiss-1000	I	-
0.220163	18.16 ± 0.07	$0.171^{+0.031}_{-0.031}$	Koshka (INASAN)/Zeiss-1000	R	-
0.230043	18.24 ± 0.09	$0.184^{+0.015}_{-0.016}$	Konkoly/RC80	r	-
0.230043	18.49 ± 0.11	$0.146^{+0.014}_{-0.016}$	Konkoly/RC80	i	-
0.245413	18.27 ± 0.09	$0.133^{+0.012}_{-0.013}$	Koshka (INASAN)/Zeiss-1000	I	-
0.249893	18.24 ± 0.07	$0.162^{+0.031}_{-0.031}$	Koshka (INASAN)/Zeiss-1000	R	-
0.250093	18.56 ± 0.04	$0.137^{+0.005}_{-0.005}$	Nanshan/NEXT	r	28324
0.267623	18.50 ± 0.05	$0.145^{+0.007}_{-0.007}$	Nanshan/NEXT	i	28324
0.272891	18.91 ± 0.05	$0.099^{+0.004}_{-0.005}$	Liverpool	g	28331
0.275143	18.31 ± 0.08	$0.115^{+0.008}_{-0.009}$	Koshka (INASAN)/Zeiss-1000	I	-
0.277891	18.55 ± 0.04	$0.138^{+0.005}_{-0.005}$	Liverpool	r	28331
0.279623	18.64 ± 0.06	$0.150^{+0.031}_{-0.031}$	Koshka (INASAN)/Zeiss-1000	R	-
0.280923	18.89 ± 0.04	$0.101^{+0.004}_{-0.004}$	Nanshan/NEXT	g	28324
0.282891	18.65 ± 0.04	$0.126^{+0.005}_{-0.005}$	Liverpool	i	28331
0.287891	18.57 ± 0.04	$0.136^{+0.005}_{-0.005}$	Liverpool	z	28331
0.304883	18.51 ± 0.11	$0.095^{+0.009}_{-0.010}$	Koshka (INASAN)/Zeiss-1000	I	-
0.309373	18.44 ± 0.09	$0.137^{+0.031}_{-0.031}$	Koshka (INASAN)/Zeiss-1000	R	-
0.334613	18.53 ± 0.09	$0.094^{+0.007}_{-0.008}$	Koshka (INASAN)/Zeiss-1000	I	-
0.339103	18.46 ± 0.09	$0.135^{+0.031}_{-0.031}$	Koshka (INASAN)/Zeiss-1000	R	-
0.375793	18.85 ± 0.12	$0.099^{+0.031}_{-0.031}$	Koshka (INASAN)/Zeiss-1000	R	-
0.400093	18.73 ± 0.08	$0.078^{+0.006}_{-0.006}$	Koshka (INASAN)/Zeiss-1000	I	-
0.452193	18.90 ± 0.08	$0.096^{+0.030}_{-0.030}$	Koshka (INASAN)/Zeiss-1000	R	-
0.602836	20.06 ± 0.12	$0.018^{+0.004}_{-0.004}$	Swift/UVOT	white	-
1.062923	> 20.4	> 0.02535	Nanshan/NEXT	r	28330
1.150123	20.37 ± 0.13	$0.020^{+0.002}_{-0.003}$	SAO RAS/Zeiss-1000	R	28322
1.167123	20.14 ± 0.10	$0.021^{+0.002}_{-0.002}$	SAO RAS/Zeiss-1000	I	28322
1.291593	20.14 ± 0.20	$0.021^{+0.004}_{-0.004}$	Koshka (INASAN)/Zeiss-1000	I	28333
1.293093	20.99 ± 0.25	$0.029^{+0.028}_{-0.028}$	Koshka (INASAN)/Zeiss-1000	R	28333
1.307923	20.99 ± 0.16	$0.015^{+0.002}_{-0.002}$	Nanshan/NEXT	r	28330
1.346603	21.01 ± 0.05	$0.014^{+0.001}_{-0.001}$	NOT	r	-
1.361891	21.17 ± 0.09	$0.012^{+0.001}_{-0.001}$	Liverpool	g	28331
1.365891	21.13 ± 0.10	$0.013^{+0.001}_{-0.001}$	Liverpool	r	28331
1.370891	21.25 ± 0.09	$0.011^{+0.001}_{-0.001}$	Liverpool	i	28331
1.375891	20.50 ± 0.08	$0.023^{+0.002}_{-0.002}$	Liverpool	z	28331
2.194383	21.54 ± 0.40	$0.007^{+0.002}_{-0.003}$	AbAO/AS-32	R	-
2.728877	22.40 ± 0.34	$0.002^{+0.001}_{-0.001}$	Swift/UVOT	white	-
2.802903	22.40 ± 0.08	$0.004^{+0.0005}_{-0.0005}$	NOT	r	-
3.15717	> 20.4	> 0.021	Mondy/AZT-33IK	R	-
5.20315	> 21.5	> 0.008	Mondy/AZT-33IK	R	-
13.070211	> 23.6	> 0.00103	MAO/AZT-22	R	-
17.077277	> 23.7	> 0.00094	MAO/AZT-22	R	-
44.561496	> 23.9	> 0.00078	MAO/AZT-22	R	-
349.653193	> 24.5	> 0.00057	MAO/AZT-22	R	-
701.205657	25.46 ± 0.35	$0.00020^{+0.00015}_{-0.00028}$	SAO RAS/BTA	R	-

References: GCN 28308 – [Pozanenko et al. \(2020\)](#), GCN 28316 – [Vinko et al. \(2020\)](#), GCN 28324 – [Moskvitin et al. \(2020a\)](#), GCN 28324 – [Zhu et al. \(2020a\)](#), GCN 28328 – [Moskvitin et al. \(2020b\)](#), GCN 28330 – [Zhu et al. \(2020b\)](#), GCN 28331 – [Izzo \(2020\)](#), GCN 28333 – [Volnova et al. \(2021\)](#)